Rapid degassing in basaltic sills as a source of Deep Long Period volcanic earthquakes

Oleg Melnik[1], Vladimir Lyakhovsky[2], and Nikolai M. Shapiro[1]

[1]Institut de Sciences de la Terre, Université Grenoble Alpes, CNRS
[2]Geological Survey of Israel

December 27, 2023

Abstract

In this paper, we present numerical modeling aimed to explain Deep Long Period (DLP) events occurring in middle-to-lower crust beneath volcanoes and often observed in association with volcanic eruptions or their precursors. We consider a DLP generating mechanism caused by the rapid growth of gas bubbles in response to the slow decompression of H\textsubscript{2}O–CO\textsubscript{2} over-saturated magma. The nucleation and rapid growth of gas bubbles lead to rapid pressure change in the magma and elastic rebound of the host rocks, radiating seismic waves recorded as DLP events. The magma and host rocks are modeled as Maxwell bodies with different relaxation times and elastic moduli. Simulations of a single sill-shaped intrusion with different parameters demonstrate that realistic amplitudes and frequencies of P and S seismic waves can be obtained when considering intrusions with linear sizes of the order of 100 m. We then consider a case of two closely located sills and model their interaction. We speculate on conditions that can result in consecutive triggering of the bubble growth in multiple closely located batches of magma, leading to the generation of earthquake swarms or seismic tremors.

Rapid degassing in basaltic sills as a source of Deep Long Period volcanic earthquakes

Oleg Melnik[1],Vladimir Lyakhovsky[2], Nikolai M. Shapiro[1]

[1]ISTerre, Université Grenoble Alpes, CNRS, Université Savoie Mont Blanc, IRD, Université Gustave Eiffel, Grenoble, France
[2]Geological Survey of Israel, Jerusalem, Israel

Key Points:

- Spontaneous bubble nucleation leads to rapid pressure increase in a batch of magma.
- Bubble nucleation in the center of a sill filled with magma results in a propagation of a nucleation front inside the sill.
- Expanding sill generate P and S seismic waves with amplitudes and frequencies close to the observations.

Corresponding author: Nikolai Shapiro, `Nikolai.Shapiro@univ-grenoble-alpes.fr`

Abstract
In this paper, we present numerical modeling aimed to explain Deep Long Period (DLP) events occurring in middle-to-lower crust beneath volcanoes and often observed in association with volcanic eruptions or their precursors. We consider a DLP generating mechanism caused by the rapid growth of gas bubbles in response to the slow decompression of H_2O–CO_2 over-saturated magma. The nucleation and rapid growth of gas bubbles lead to rapid pressure change in the magma and elastic rebound of the host rocks, radiating seismic waves recorded as DLP events. The magma and host rocks are modeled as Maxwell bodies with different relaxation times and elastic moduli. Simulations of a single sill-shaped intrusion with different parameters demonstrate that realistic amplitudes and frequencies of P and S seismic waves can be obtained when considering intrusions with linear sizes of the order of 100 m. We then consider a case of two closely located sills and model their interaction. We speculate on conditions that can result in consecutive triggering of the bubble growth in multiple closely located batches of magma, leading to the generation of earthquake swarms or seismic tremors.

1 Plain Language Summary

Volcano seismology is one of the main geophysical methods used to study volcanic processes and to forecast the eruptions. It is based on analysis of ground motion recorded by seismographs installed in the vicinity of volcanoes. Different seismic signals such as impulsive volcanic earthquakes and nearly continuous volcanic tremors are recorded during periods corresponding to preparation of eruptions. Some of them originate from depths of a few tens of kilometers, i.e., from the roots of the system that feeds the magma supply to volcanoes and their eruptions. Therefore, such deep seismic sources are particularly interesting because they may represent early eruption precursors. While we still lack physical understanding of the processes leading to this deep volcanic seismicity, there are several reasons to consider that it is not caused by a sudden slip on faults responsible for the majority of "regular tectonic" earthquakes. In this paper, we use numerical simulations to test another possible mechanism of generation of deep volcanic earthquakes. Namely, we assume that they can be caused by rapid growth of bubbles from the gas that was initially dissolved in the magma. We use numerical simulations to demonstrate that this model predicts main properties of the observed seismic signals.

2 Introduction

Degassing is one of the main driving forces behind the volcanic activity. The separation of gas and melt phases leads to the formation of bubbles, whose presence increases the magma buoyancy thereby leading to its ascent. Degassing is very strong at the very top part of volcanic systems where most of gases, especially H_2O, no longer remain dissolved due to the pressure decrease (e.g., Wallace et al., 2015). Therefore, dynamics of gas bubbles in the magma is predominant during the eruptions (e.g., Jaupart & Vergniolle, 1988; Cassidy et al., 2018) and other near-surface volcano-related processes. In particular, the degassing and associated bubble growth can cause significant magma pressure variations. If these pressure perturbations are sufficiently rapid, they are transmitted into the surrounding elastic media as seismic waves that can be recorded by seismographs as volcanic earthquakes. Such rapid pressure changes can occur when a magma volume first reaches the saturation level and then achieves the critical supersaturation after which the gas bubbles nucleate and grow rapidly (Lyakhovsky et al., 1996; Lensky et al., 2006).

In one scenario, a rapid decompression of a shallow intrusion caused by a sudden gas escape via conduit results in a critical magma supersaturation. This pressure drop is fallowed by a pressure recovery because of the gas bubble grows (Nishimura, 2004). B. Chouet et al. (2006) modeled such sequence of magma depressurisation-pressurisation and related elastic deformation of the surrounding rocks in order to explain very long period seismic signals associated with the Vulcanian explosions at Popocatépetl Volcano in Mexico (B. Chouet et al., 2005). They considered a sill-shaped volume of rhyolitic magma at a depth of 1.5 km. The system response has been found to depend strongly on various parameters such as volatile diffusivity in the melt, the bubble number density, the initial bubble radius, and the shape of the intrusion. The model could reasonably explain observed seismic waveforms within the range of acceptable parameters and predicted pressure variations of the order of a few MPa with characteristic timescale of tens of seconds.

Another scenario has been recently considered by O. Melnik et al. (2020) to explain the Deep Long Period (DLP) earthquakes occurring in middle-to-lower crust beneath volcanoes and often associated with eruptions or their precursors (e.g., Ukawa & Ohtake, 1987; Pitt & Hill, 1994; White et al., 1996; Power et al., 2004; Nichols et al., 2011; Aso et al., 2013; Aso & Tsai, 2014; Shapiro, Droznin, et al., 2017; Hensch et al., 2019; Kurihara et al., 2019; Wech et al., 2020; Ikegaya & Yamamoto, 2021; Kurihara & Obara, 2021; Greenfield et al., 2022; Lu & Bostock, 2022; Song et al., 2023). In some cases, the origin of these DLP earthquakes has been attributed to the processes occurring within a cooling magma body stalled beneath the crust such thermal stresses (Aso et al., 2013) or "second boiling", i.e., repeated pressurization by volatiles exsolution during magma crystallization (Wech et al., 2020). However, such cooling-related mechanisms are unlikely for DLP events occurring beneath active volcanoes in association with eruptions. Therefore, O. Melnik et al. (2020) suggested a possible DLP generating mechanism related to the rapid growth of gas bubbles in response to the slow decompression of oversaturated magma. In this model, a volume of magma saturated with H_2O–CO_2 volatiles is slowly rising up which causes its depressurisation. This magma first reaches the saturation level and then achieves the critical supersaturation after which gas bubbles nucleation causes rapid pressure and elastic stress variations resulting in seismic waves recorded as DLP earthquakes.

The model of O. Melnik et al. (2020) was particularly aimed to explain the DLP earthquakes occurring beneath the Klyuchevskoy volcano in Kamchatka, Russia (e.g., Fedotov et al., 2010; Shapiro, Sens-Schönfelder, et al., 2017; Koulakov et al., 2020) just beneath the crust-mantle boundary (Levin et al., 2014; Shapiro, Droznin, et al., 2017; Galina et al., 2020; Journeau et al., 2022) at a depth of approximately 30-35 km. Recent studies suggested that primary Klyichevskoy magma may contain more than 4 wt% H_2O and 0.35–0.9 wt% CO_2 (Portnyagin et al., 2007; Mironov & Portnyagin, 2011; Portnyagin et al., 2019). Single H_2O volatile phase would result in a small saturation depth, but the addition of 0.6 wt% of CO_2decreases volatile solubility dramatically (Papale, 1999; Burgisser et al., 2015) so that magma becomes super-saturated at pressures of above 800 MPa (30 km depth).

O. Melnik et al. (2020) have shown that for realistic magma compositions and values of the gas and bubble content, the elastic deformation of surrounding rocks forced by the expanding bubbly magma can be fast enough to generate seismic waves. They approximately estimated a volume of degassing magma of $\sim 10^3 - 10^4 m^3$ would be necessary to explain amplitudes of signals recorded from the DLP earthquakes beneath the Klyuchevskoy volcano. Nevertheless, this model contained important approximations. First, an instantaneous bubble nucleation in the whole batch of magma was assumed, similar to B. Chouet et al. (2006). However, such scenario is unlikely within the slowly uplifting magma batch. In this case, we can rather expect that the babble growth will be first triggered in a small volume and than spontaneously propagate through the rest of the magma body. Second limitation of O. Melnik et al. (2020) was that only a spherical-shape intrusion was modeled. Also, excitation of seismic waves was not explicitly computed and the amplitudes of seismograms were predicted based on a simplified approximation.

To overcome the mentioned shortcomings, we developed a more complete and accurate model of generation of seismic waves by the pressure variations caused by bubbles growth in magma. The model is based on an accurate numerical solution of coupled fluid-elastic equations and includes: (1) a bubble nucleation front propagating from initial trigger point, (2) a sill-shape magma intrusion, and (3) an exact estimation of the associated seismic potency (moment) tensor in order to compute the seismograms.

We start with formulating the mechanical model in section 3. A particular attention is payed to an accurate description of the compressibility of the bubbly magma and its variations in association with the bubble growth. We then apply the developed mechanical framework to model the gas bubble growth in an intrusion shaped as a horizontal sill. The numerical implementation and model settings are described in section 4. The results of the modeling are presented in section 5 and their implications are discussed in section 6. In particular, after considering solutions for a single sill-shaped intrusion with different parameters, we introduce a case of two closely located sills and model their interaction. We then speculate how such interaction can result in consecutive triggering of the bubble growth in multiple closely located intrusions and lead to generation of earthquake swarms or seismic tremors.

3 Mechanical model of a DLP earthquake source

3.1 Conceptual model

We consider a scenario illustrated in Figure 1a. Basaltic magmas rising from the mantle are underplated beneath the Moho forming sill-shaped intrusions. Following O. Melnik et al. (2020), we consider that H_2O-CO_2 rich basaltic magma becomes oversaturated at these depths leading to a spontaneous nucleation and rapid growth of gas bubbles within the sill (Figure 1b). Magma degassing in an initial small volume leads to perturbations of the pressure in its vicinity that, in turn, results in nucleation and growth of new bubbles. Such "nucleation" front propagates along the whole sill (Figure 1c) causing it expansion (Figure 1d) and leading to elastic deformation of the surrounding rocks and generation of seismic waves that are then recorded by seismographs installed at the surface.

3.2 Mathematical formulation for a coupled fluid-solid system with bubbles

The mechanical model for the scenario described above consists of a sill-shaped cavity filled with a viscous fluid (magma) embedded in an elastic medium (rocks). We solve the equations of motion for a continuum media in the whole volume of the model without body force:

$$\rho \frac{\partial^2 u_i}{\partial t^2} = \frac{\partial \sigma_{ij}}{\partial x_j} \tag{1}$$

where ρ – material density; u_i – displacement vector; σ_{ij} – stress tensor. The total strain is calculated from the displacement field as:

$$\varepsilon_{ij}^t = \frac{1}{2}\left(\frac{\partial u_i}{\partial x_j} + \frac{\partial u_j}{\partial x_i}\right) \tag{2}$$

Different stress–strain constitutive relations (different rheology) are adopted for the magma and the surrounding material. The host rock is simulated as perfectly elastic isotropic Hookean solid ($\varepsilon^t = \varepsilon^e$, where index e corresponds to elastic deformations). The constitutive stress-strain relations for elastic deformations are:

$$\sigma_{ij} = \lambda \varepsilon_{kk}^e \delta_{ij} + 2\mu \varepsilon_{ij}^e \tag{3}$$

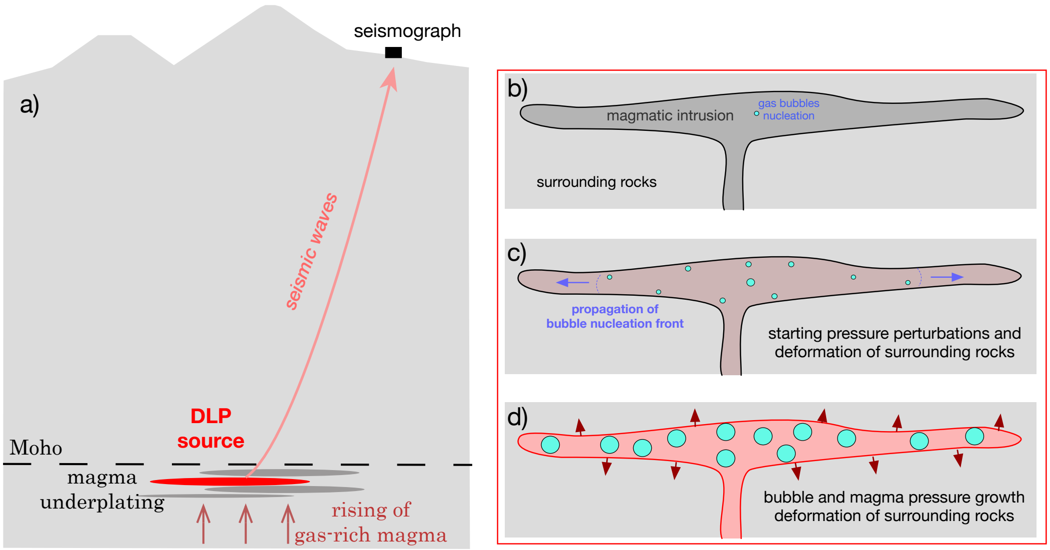

Figure 1. Schematic representation of the DLP source model. (a) General geometry with a source (a sill filled with a rapidly degassing magma highlighted with the red color) located at the crust-mantle boundary and the station recording seismic waves located at the surface. (b)-(d) Main stages of the rapid degassing of the magma within a sill.

where λ and μ are Lame elastic modulus.

Magma is approximated by Maxwell visco-elastic body with the total strain, ε^t_{ij}, being a sum of the elastic, ε^e_{ij} and irreversible, ε^{irr}_{ij}, strain components.

$$\varepsilon^t_{ij} = \varepsilon^e_{ij} + \varepsilon^{irr}_{ij}, \tag{4}$$

Adopting the Newtonian stress – strain-rate relations for a viscous fluid, the deviatoric stress, $\tau_{ij} = \sigma_{ij} + P\delta_{ij}$ (where $P = -trace(\sigma_{ij})/3$ is the pressure) we obtain:

$$\tau_{ij} = \eta \frac{\partial \varepsilon^{irr}_{ij}}{\partial t}, \qquad \varepsilon_v = P/K \tag{5}$$

where η is the melt viscosity. The volumetric strain component ε_v for the bubble-free magma is calculated using the magma compressibility K. The magma remains bubble-free until the pressure is above the critical value associated with super-saturation of the gas dissolved in the melt.

As soon as the critical magma super-saturation is reached, bubbles nucleate and start to expand. The dynamics of bubble growth under various conditions have been widely discussed in the literature (see reviews by (Sparks, 1978; Gardner et al., 2023) and references therein). According to the bubble growth model (Lyakhovsky et al., 1996) the gas diffusion into the small bubble is very efficient at the initial stage of growth following the nucleation. The initial pressure difference or nucleation pressure is partly compensated by the surface tension term, which decreases as inverse of the bubble radius, $1/R$. The surface tension steeply decreases with the bubble growth and the pressure driving the bubble expansion practically remains constant. At this stage, the exponential increase of the bubble radius is controlled by the viscosity of the surrounding melt and the nucleation over-pressure $\Delta P = P_s - P_0$ or the difference between the saturation pressure, P_s, and the pressure in the surrounding melt, P_0. With the increase of the bubble radius, the efficiently of the diffusion decreases, and the rate of the bubble growth is controlled by the diffusive gas flux from the surrounding melt cell with a radius S. Finally, the bubble size and gas pressure approach their equilibrium values depending on the initial values of pressure, gas concentration, and cell size, as well as melt properties. The initial cell size, S_0, or the melt volume surrounding every bubble may be calculated assuming certain number of bubbles nucleated from the unit melt volume, or bubble number density, N_d:

$$\frac{4}{3}\pi S_0^3 = \frac{1}{N_d} \tag{6}$$

The details of a single bubble growth model developed by (O. Melnik et al., 2020) consists of Raleigh-Lamb equation coupled with diffusion equations for multiple dissolved volatile and is briefly discussed in Appendix Appendix A.

The pressure inside the bubble P_g just after nucleation is equal to the saturation pressure P_s. It is several tens of MPa higher than the initial pressure in the surrounding melt P_0. At final stage of the bubble growth both gas and melt P_m pressures approaches to the equilibrium pressure, P_{eq}. We can define the pressure in the bubbly magma P_b as:

$$P_b = P_g\alpha + P_m(1-\alpha), \tag{7}$$

where α is the volume fraction of bubbles, $\alpha = \frac{R^3}{S_0^3}$.

Figure 2 shows the overpressure, $P_b - P_0$, evolution in the bubbly magma pocket simulated by the model from O. Melnik et al. (2020) for three different values of the bubble number densities, $N_d = 10^{13}/m^3$ (green line), $N_d = 10^{14}/m^3$ (red line), $N_d = 10^{15}/m^3$ (blue line). Here we use the initial over-pressure of $\Delta P = P_s - P_0 = 40$ MPa (Shea, 2017). This pressure increase leads to a deformation of the surrounding rock mass and serves as a source pressure for the sill opening. The S-shape of the pressure curves could be well approximated by an exponential function:

$$P_b = P_{eq} - (P_{eq} - P_0) * exp(b * \delta t^\gamma) \tag{8}$$

where δt is time since the bubble nucleation; $\gamma = 2.4$. The fitting coefficient b significantly depends on the assumed bubble number density. The fitted values are: $b = -28$ for $N_d = 10^{13}/m^3$, $b = -187$ for $N_d = 10^{14}/m^3$, and $b = -1355$ for $N_d = 10^{15}/m^3$. Figure 2 shows the comparison between calculated and fitted pressure variations for different number density of bubbles.

The equilibrium pressure in the melt pocket depends on the deformation of the surrounding rock and volume change of the considered bubbly melt pocket. It is calculated using the mass conservation law of the gas, stored in the bubble and dissolved in the surrounding melt, $m_g = Const.$:

$$m_g = \frac{4}{3}\pi S_0^3 C\rho_m + \frac{4}{3}\pi R^3\rho_g = \frac{4}{3}\pi S_0^3 C_s\rho_m \tag{9}$$

where C_s is the gas concentration at the super-saturation needed for the bubble nucleation, ρ_m is the melt density. We use linear approximation for gas density, ρ_g:

$$\rho_g = a_r(P - P_0) + b_r \tag{10}$$

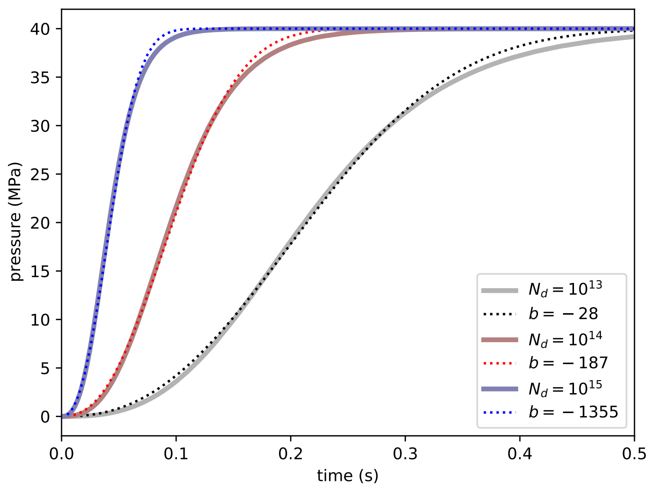

Figure 2. Comparison between calculated and fitted pressure variations for different number density of bubbles

and solubility, C:

$$C = a_c(P - P_0) + C_0 \tag{11}$$

with the following values: $a_c = 1.4410^{-5}/MPa$, $a_r = 0.586kg/m^3/MPa$ $b_r = 419.0kg/m^3$. The value of C_0 defines the volatile concentration at pressure P_0.

Substituting these linear approximation into the gas mass balance equation (9)

$$S_0^3\rho_m\left(a_c(P_{eq} - P_0) + C_0\right) + R^3\left(a_r(P_{eq} - P_0) + b_r\right) = S_0^3\rho_m(a_c(P_s - P_0) + C_0) \tag{12}$$

and dividing by S_0^3 leads to:

$$\rho_m\left(a_c(P_{eq} - P_0) + C_0\right) + \alpha\left(a_r(P_{eq} - P_0) + b_r\right) = \rho_m(a_c(P_s - P_0) + C_0) \tag{13}$$

By solving equation (13) against P_{eq} we obtain the relation that adjusts equilibrium pressure in equation (8)

$$P_{eq} = \frac{\rho_m a_c P_s + \alpha(a_r P_0 - b_r)}{\alpha a_r + a_c\rho_m} \tag{14}$$

Equation (8) together with (14) govern the evolution of the source pressure in the bubbly magma. As soon as the nucleation condition is reached in particular cell instead of using equation (5) to calculate the pressure from volumetric strain, we assume that the pressure is specified by equation (8) and the volume fraction of bubbles is calculated as a difference between the total volume change and the elastic melt expansion:

$$\alpha = \varepsilon_v - P_b/K; \tag{15}$$

The equilibrium pressure is then calculated from equation (14). Obtained P_{eq} and re-calculated P_b values are used for the time marching.

If this deformation is sufficiently rapid, the seismic waves are transmitted into the surrounding elastic media and recorded by seismographs as volcanic earthquakes. The earthquake source mechanism is estimated by integrating the irreversible strain over the sill volume:

$$\Pi_{ij}(t) = \int_V \varepsilon_{ij}^{irr}(t) d^3x \tag{16}$$

Following Ben-Menahem and Singh (2012) this tensor is called potency or geometrical moment. The time-dependent moment tensor components are calculated using the Hook stress-strain relations with Lame parameters λ and μ of the host rock:

$$M_{ij}(t) = \lambda \Pi_{kk} \delta_{ij} + 2\mu \Pi_{ij} \tag{17}$$

Synthetic seismograms are then computed as a convolution of the time-dependent seismic moment with the Green's function. For the latter we use the far-field P and S waves in a homogeneous elastic media (Aki & Richards, 2002). The near-field terms of the Green's function are ignored because the source-receiver distance is significantly larger than the wavelengths at dominant frequencies (above 1 Hz).

4 Numerical method and model settings

The 3D numerical modeling was performed using Explicit Finite Difference Lagrangian method, based on the FLAC (Fast Lagrangian Analyze of Continua) algorithm originally developed by Cundall (1988) for elasto-plastic rheology and implemented in the ITASCA software. The FLAC algorithm was modified for visco-elastic media (Poliakov et al., 1993). A modified version of this code incorporating heat transport is known as PAROVOZ and is widely used by many researchers. Lyakhovsky et al. (2001) developed their own 3-D code for quasi-static visco-elastic damage rheology modelling, which was used in many geodynamic applications. Later on the code was modified for dynamic processes, by reducing force damping to realistic values corresponding to wave attenuation. The numerical time-step was defined according to the Courant–Friedrichs–Lewy stability condition for explicit time-marching simulations. Technical details of the numerical approach for dynamic modelling of seismic wave propagation were discussed by Lyakhovsky et al. (2016).

We considered several cases of the model geometry. Most of simulations were performed for the model volume 200x200x100 m with a 50 m radius and 3 m thick penny-shaped sill located in the center (Figure 3a). In a few cases the model size have been doubled (both model dimensions and sill radius) keeping the same thickness. In the last series of the model runs two penny-shaped sills with 40 meter radius located in the same plain with three different distances, 40, 45, 50 m., between their edges (Figure 3b). The adaptive grid with tetrahedral elements with 0.5 meter grid step represents the sill volume. The grid size gradually increases in vertical direction away from the sill.

Equation (1) is solved with fixed zero displacement boundaries with attached narrow layer of highly damping material that prohibits the reflection of waves traveling inside the host rock. The initial stress is equal to the solubility pressure P_0 and zero deviatoric components.

The elastic material surrounding the sill has the properties close to those of the mantle: the density $\rho = 3000\, kg/cm^3$, bulk modulus K of 80 GPa, and rigidity (shear modulus) μ of 50 GPa. With these properties the seismic wave velocities in the host rock are: V_p=7 km/s, V_s=4.1 km/s. The density of the melt inside the sill is $\rho_m = 2800\, kg/cm^3$,

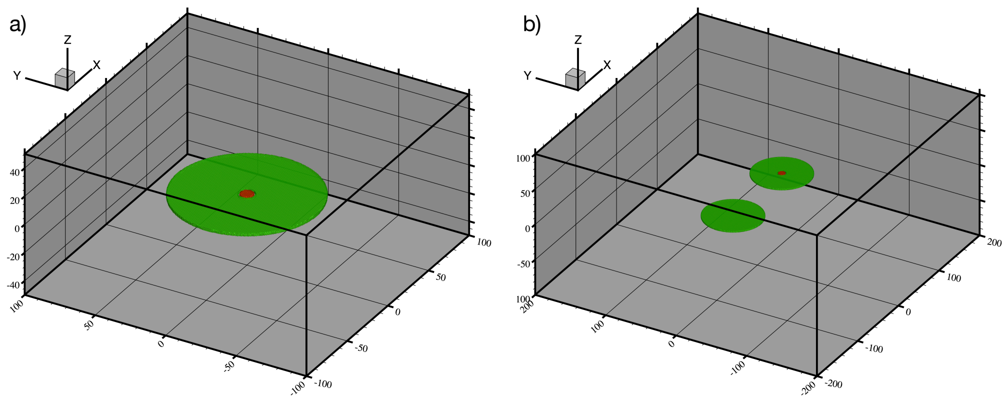

Figure 3. Geometries used in numerical simulations. (a) A penny-shaped sill of 50 m radius and 1 m thickness. Red color show the volume in which the bubble grow is triggered. (b) Two penny-shaped sill of 40 m radius and 1 m thickness. The bubble growth is triggered in the center one of the sills as shown with red color.

bulk modulus 10 GPa, and very low rigidity (5 orders of magnitude below the host rock rigidity). Melt viscosity (η) varied between 10 and 10^3 Pa*s between different model runs. These values provide numerical stability of the Maxwellian visco-elastic solution with negligibly small elastic shear strain components in the melt. The shear stress in the melt is controlled by the product of the strain rate and melt viscosity, like in the Newtonian fluid. For the small volume fraction of bubbles the magma viscosity variations due to bubble content might be neglected. During the simulation the event potency is calculated by integrating the inelastic strain over the volume of the sill (equation 16).

After estimating the potency tensor, we compute the propagation of seismic waves through the crust with average density of 2900 kg/m^3 and P and A wave velocities of 6062 and 3500 m/s, respectively. We consider a source-receiver distance of 40 km and a take-off angle at the source of 30°. This approximates the geometry with a curved seismic ray reaching a station located nearly above the source.

5 Results

During the study we considered fifteen different models (see Table 1), twelve of them for a single sill (Figure 3a) and the last three for two discs (Figure 3b). All the simulations start with a spontaneous bubble nucleation in the 5 meter circle area located in the center of the sill (red zone in Figure 3). In the case of a non-deformable surrounding material and adopted melt parameters the maximal over-pressure may grow up to about 40 MPa in respect of the initial pressure P_0. However, its final value is significantly reduced because of the elastic deformation of the surrounding rock and the increase of the sill volume (see equation (14).

5.1 Single sill configuration

Figure 4 shows four horizontal and vertical cross sections for sequential snapshots of pressure evolution for model N1-B (see Table 1 for parameters). Dashed lines on each cross section indicate the boundaries of the magmatic sill, where the bubble nucleation is expected.

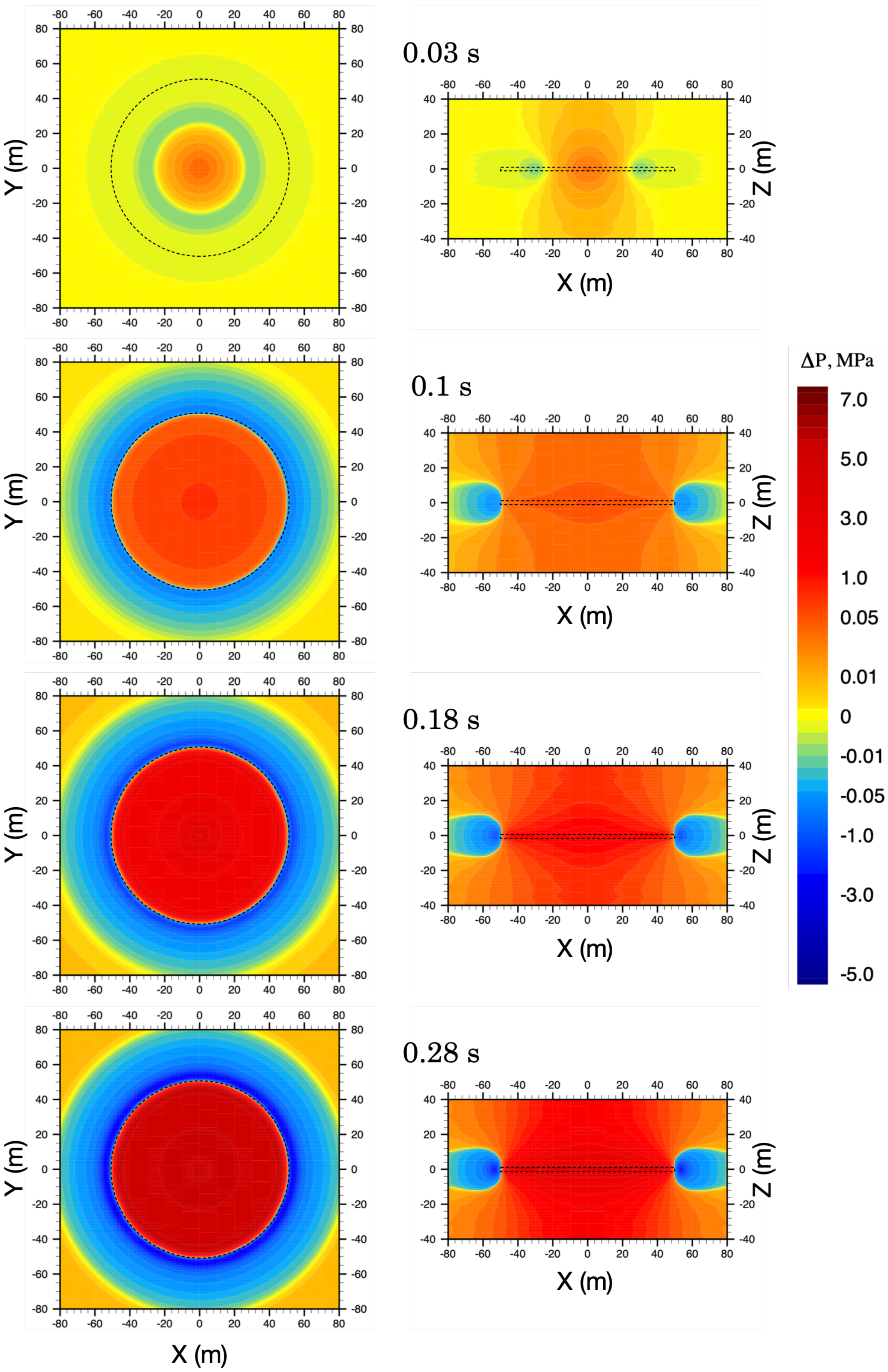

Figure 4. Snapshots of pressure evolution in time in a model N1-B. Left and right frames show horizontal and vertical cross-sections at Z=0 and Y=0, respectively. Time is indicated above the frames.

Run #	Model ID	Sill size m	Nd $1/m^3$	Nucleation threshold, kPa	Melt viscosity Pa s	Potency m^3
1	N1 A	50	10^{13}	10	100	22.325
2	N1 B	50	10^{13}	30	100	21.692
3	N1 C	50	10^{13}	50	100	20.238
4	N2 A	50	10^{14}	10	100	22.286
5	N2 B	50	10^{14}	30	100	22.133
6	N2 C	50	10^{14}	50	100	21.895
7	N3 A	50	10^{15}	10	100	22.121
8	N3 B	50	10^{15}	30	100	21.875
9	N3 C	50	10^{15}	50	100	21.651
10	N1 B V01	50	10^{13}	30	10	22.300
11	N1 B V10	50	10^{13}	30	1,000	22.359
12	N1 B L100	100	10^{13}	30	100	100.41
13	N4 1	2x40 Dist. 120	$3\ 10^{13}$	20	100	28.686
14	N4 2	2x40 Dist. 125	$3\ 10^{13}$	20	100	28.167
15	N4 3	2x40 Dist. 130	$3\ 10^{13}$	20	100	14.391

Table 1. Run parameters

During the early stage of the pressurization in the nucleated zone (reddish colors), the sill opening results in the decreased fluid pressure around this zone (bluish colors) leading to new nucleation and bubble growth. The location of the narrow yellow ring between these zones corresponds to the radially propagating bubble nucleation front. The front expansion is driven by the "crack waves" resulting from elastic-acoustic coupling on the sill boundaries an propagating along the sill (e.g., B. Chouet, 1986; B. A. Chouet, 1996). The exact cylindrical symmetry is preserved during the sill expansion since the melt and surrounding rocks are homogeneous. The size of the area with the elevated pressure where the bubble are nucleated is about 20 m for the first snapshot and the nucleation front reaches the sill edge (50 meter) during 0.1 s. This means that the nucleation front propagates at the rate of about 0.5 km/s.

Seismic source properties, synthetic seismograms, and their Fourier amplitude spectra for model N1-B are shown in Figure 5. As expected for vertically expanding horizontal sill, the potency tensor is dominated by the ZZ component. Its conversion into seismic moment with equation (17) results in a diagonal tensor with ZZ component approximately three times larger than YY and XX (e.g., pure horizontal tensile crack). All three non-zero moment tensor components are proportional to the ZZ potency function whose time dependence defines the source time function. The body wave displacement and velocity is proportional to its first and second time derivatives, respectively. The latter, shown in Figure 5b is dominated by a low-frequency pulse corresponding to the kinetics of the bubble growth. Much weaker high frequencies correspond to bouncing of the "crack waves" withing the sill (e.g., B. A. Chouet, 1996). Resulting synthetic seismograms (Figure 5c) contain both P and S waves with amplitudes close to the observations. Their frequency content is also close to the observations (Figure 5d). The relatively long coda seen in the observed signal and not reproduced in the synthetic seismograms most likely arises from the scattering of seismic waves within the heterogeneous volcanic media, i.e., from the propagation effect whose explanation would require using a more realistic Green's function.

For other cases with higher N_d values, the nucleation front propagates two (N2 series) and even more than three (N3 series) times faster. The bubble nucleation in the whole sill occurs relatively fast (0.1 s), while the overall duration of the sill expansion

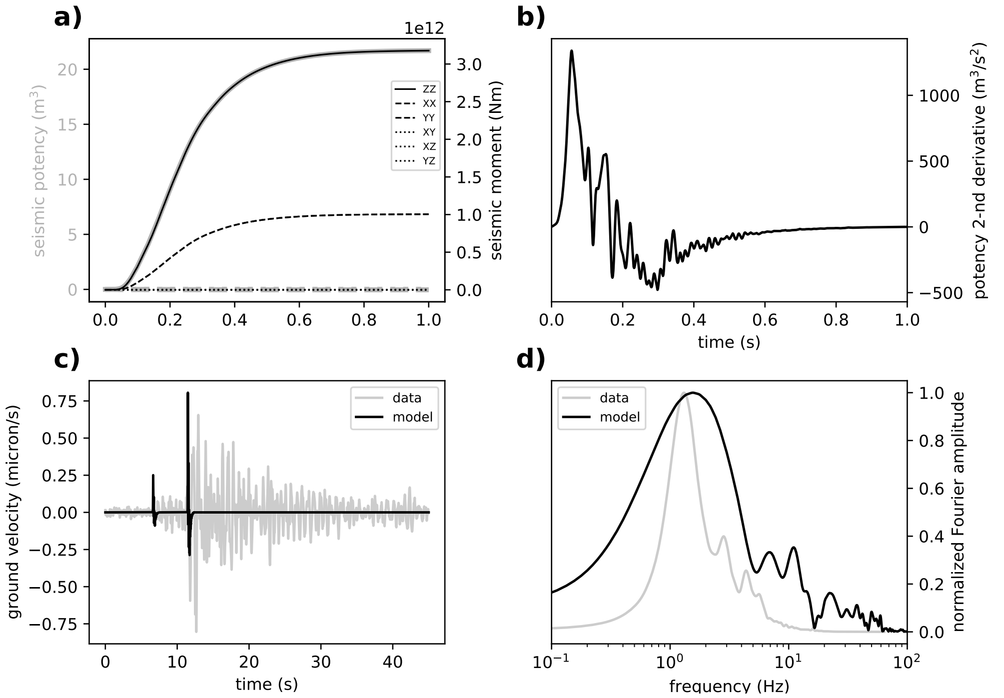

Figure 5. Seismic signature of model N1-B. (a) Components of potency (thick gray lines) and seismic moment (thin black lines) tensors as function of time. (b) Second derivative of the ZZ potency function. (c) Comparison of synthetic and observed seismograms shown with black and gray lines, respectively. East-component seismogram of a DLP earthquake occurred on June 26, 2012 recorded at station LGN located on the slope of the Klyuchevskoy volcano (see supplementary material for details) is shown as "data" (signal was high-passed at 0.5 Hz to remove the microseismic noise. (d) Normalized Fourier amplitudes of signals shown in (c) smoothed in a 1 Hz wide moving window.

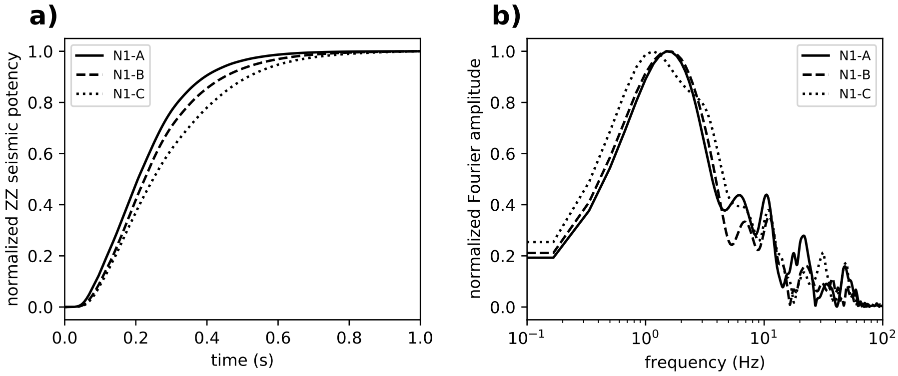

Figure 6. Influence of nucleation threshold ΔP on seismic source time functions. Three considered models differ by the value of this parameter: N1-A 10 kPa, N1-B 30 kPa, N1-C 50 kPa. (a) ZZ components of the seismic potency tensors as function of time. (b) Normalized Fourier amplitude of second derivatives of the ZZ potency function.

vary between 0.2 and 0.8 s for the series of nine model setting (lines 1-9 in Table 1). Therefore, the overall duration is mainly controlled by the kinetics of the bubble growth. The nucleation of new bubbles under appropriate conditions occurs extremely fast and the nucleation time scale is well below the time scale of the front propagation (for the discussed sill size) and future sill pressurization.

The bubbles nucleate when the over-saturation pressure is exceeded (e.g., Hirth et al., 1970). The level of the super-saturation depends on the temperature and a number of melt properties including surface tension, volume, and concentration of water molecules in the melt, as well as distance between them, diffusion coefficient of volatiles at the bubble-melt interface, probability that a nucleus at the top of the barrier will go on to form the new phase, rather than dissolve (Zeldovich factor), and others. With a huge uncertainty of these parameters and difficulties in their experimental constrain, we used three different values of the bubble number density ($N_d = 10^{13}$, 10^{14}, and 10^{15} $1/m^3$) and super-saturation thresholds ($\Delta P = 10$, 30, and 50 kPa), assuming instantaneous nucleation when the target super-saturation is reached. Comparison of time-dependent potency for different simulations demonstrate that the pressurization rate weakly depends on the nucleation threshold, ΔP (Figure 6), and it is strongly affected by the bubble number density,N_d (Figure 7). The general pattern of the evolving pressure is very similar to the one shown in Figure 5, but differs only by the rate of pressurization. The sill expands significantly faster in the case with elevated N_d values.

Two additional simulations (10, 11 in Table 1) were performed to study a possible impact the melt viscosity, which was increased and decreases by an order of magnitude covering the realistic range of the basaltic melt properties. The difference in the pressurization rate (potency increase, not shown here) between these two cases and the model N1-B is negligibly small. The rate of the magma flow becomes important only at high viscosities (above 10^5 Pa s) typical for rhyolitic magmas (Hess & Dingwell, 1996) and controls the rate of sill pressurization.

Similarly to the classical seismological scaling relations we expect stronger event with larger potency (area times opening) proportional to the sill size. For the same pressure inside the sill with radius increased by a factor of two, we expect the sill opening to increase by a factor $\sqrt{2}$, since penny-shaped crack opening is scaled as square root of the disc radius. Together with four times area increase (size in a power two), the potency should increase by a factor $2^{2.5} \approx 5.66$. However, opening of the sill leads to the reduc-

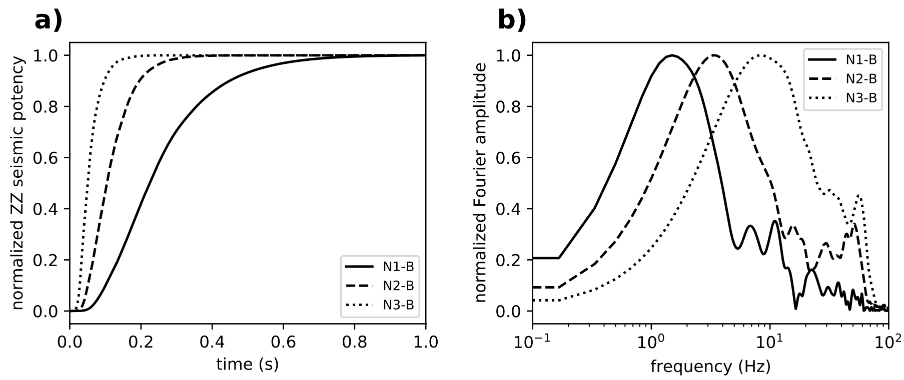

Figure 7. Influence of bubble number density N_d on seismic source time functions. Three considered models differ by the value of this parameter: N1-B 10^{13}, N1-B 10^{14}, N3-B 10^{15}. (a) ZZ components of the seismic potency tensors as function of time. (b) Normalized Fourier amplitude of second derivatives of the ZZ potency function.

tion of the equilibrium pressure of the bubbly magma inside the sill. The results of the model N1-B-L100 show that the potency for the 100 m sill, instead of 50 m, is about 100 m^3 meaning the increase by a factor 5 instead 5.66. The coupling between opening and pressure in the sill leads to a potency-area scaling with slightly deviates from the predictions of the linear elasticity ignoring the pressure-size dependency.

5.2 Configuration with two sills

Expansion of the sill due to the bubble growth and pressurization leads to the deformation of the surrounding elastic media and formation of a relatively wide zone with a reduced pressure clearly seen in the last snapshots of Figure 4. This pressure reduction can initiate bubble nucleation in another sill or magma pocket located at a certain distance within the area of the negative pressure change (blue zone). Three last simulations demonstrate the sensitivity of the secondary nucleation to the distance between two discs (Figure 3b). In order to improve the numerical resolution without significantly increasing the computation time, we slightly decreased the disc radius to 40 m and placed the second disc at three different distances between their centers 130, 120, and 125 m (Table 1) or 50, 40, and 45 m between disc edges. Figure 8 shows the snapshots for the case N4-1. Slightly before 0.3 s the nucleation threshold (20 KPa) is achieved in the disc on the left and the nucleation starts on the right edge of this disc mostly affected by the pressurization of the first disc (snapshot 1 in Figure 8).

Seismic response of a two-sill system is illustrated in Figure 9 for model N4-2 (separation of 125 m). Nucleation of the first sill results in the initial rise of potency/moment values occurring between 0 and 0.3 s. This initial pulse is shorter that for model N1-B (Figure 5) and the dominant frequency higher mainly because of the smaller sill size. The bouncing of “crack waves” expressed in high frequencies seems to be more prominent in such smaller sill. The second sill nucleation starts at 0.6 s. The overall potency increases corresponding to two sills are nearly identical. At the same time, the second derivative of the potency function shows that the second impulse is relatively depleted in high frequencies. The reason for this is that the nucleation of the second sill starts not at the center but at the edge. As a result, the bouncing of “crack waves” is much less efficient.

The time delay for the second sill nucleation strongly depends on the distance between discs as shown in Figure 10. It increases from 0.3 to 0.6 s between separations of 120 ans 125 m. For the 130 m distance between disc centers, the nucleation threshold is never achieved. After the nucleation occurred, the nucleation front propagates toward the opposite edge of the disc with the rate controlled by the bubble growth parameters as discussed above. With pressure growth increase in both discs, the size of zone with a reduced pressure (blue colors) increases and may provoke nucleation in additional magma pockets, not necessarily aligned in the same plane. Vertical cross sections clearly demonstrate significant increase of the negative pressure zone in the Z-direction. Comparison between three cases of the N4 series shows that there exist certain critical distance for the secondary nucleation and the delay time strongly depends on this distance.

6 Discussion and conclusions

We developed an accurate model of generation of seismic waves by the pressure variations caused by bubble growth in the magma. This model is based on a numerical solution of a fluid-elastic coupled equations and includes a bubble nucleation front propagating from initial trigger point in a sill-shaped magma intrusion.

The results of our simulations confirm the hypotheses of O. Melnik et al. (2020) that the rapid growth of gas bubbles within magmatic intrusions can generate seismic waves with amplitudes and spectral content similar to those observed from DLP earthquakes. In particular, we show that with modeling realistic shapes of the intrusions such as sills, a mostly volumetric expansion results in generation of stronger S waves than P waves. Our simulations show that realistic amplitudes can be predicted with modeling sills of ∼50 m of radius and ∼1 m of thickness. The object of such dimensions can correspond either to an individual small sill or to a pocket of oversaturated magma within larger intrusions.

Additionally, our modeling shows that bubble nucleation front propagation is controlled by the coupled elasto-acoustic waves. This propagation is rapid comparing to the kinetics of the bubble growth. The later dominates the source time function and the spectral content of the emitted signals. This kinetics is controlled by the the bubble number density N_d and the gas content in the magma (O. Melnik et al., 2020). The effect of bouncing of "crack waves" eventually leading to resonances of fluid filled cracks (e.g., B. Chouet, 1986; B. A. Chouet, 1996; Maeda & Kumagai, 2017) is rather weak and is not necessary to explain the properties of the observed DLP signals.

The results of our modeling presented in subsection (5.2) highlight a possibility of "interaction" between closely located intrusions when the elastic deformation caused by the degassing/expansion of the first sill can trigger the bubble nucleation in the next closely located magma pocket. We presented simulations for two "interacting" sills. This results can be extrapolated to a case of many closely located magma pockets acting in a cascade. Such behavior can explain the observation of DLP earthquakes often occurring as swarms of many events closely located in time (e.g., White et al., 1996; Shapiro, Droznin, et al., 2017; Song et al., 2023) eventually leading to emergence of deep volcanic tremors (e.g., Aki & Koyanagi, 1981; Soubestre et al., 2019; Journeau et al., 2022).

The emergence of tremors would become favorable in a configuration where many "interacting" pockets of oversaturated magma are closely located. The results shown in Figure 10 demonstrate that with the selected model parameters and in approximation of in-plane circular sills, the interaction becomes possible when inter-sill distance approaches the sill radius. The "interaction" distance would then increase with decreasing the the nucleation threshold. The time delay between two "interacting events" would increase with increasing the inter-sill distance and also with decreasing the bubble number density.

More generally, some scaling relations based on the stress distribution around a pressurized inclusion could be considered. The linear elasticity predicts that the pressure distribution around the inclusion is proportional to the overpressure and decreases as a polynomial function of the ratio $\frac{R}{d}$ (R – disc radius, d – distance from the inclusion center). Near the edge of the inclusion the forth order term, $(\frac{R}{d})^4$, is dominant and defines fast pressure decay away from the inclusion. The width of the zone with the negative pressure is expected to be of the order of the inclusion size. For a given distance, d, from the inclusion, the nucleation occurs when the pressure in the inclusion drops below certain critical value, which linearly increases with the nucleation threshold and decreases as $(\frac{R}{d})^4$, which is the dominant term for the near-field solution.

The presented modeling frameworks can be applied to magma pockets of arbitrary shapes. One possible direction of its application to better understand the origin of deep volcanic tremors would be to investigate the cascading of magma degassing in a system containing many sills and dykes with variable sizes (e.g. O. E. Melnik et al., 2021; Bindeman et al., 2023). A more challenging and important task would be to move from a "static" systems of interacting magma pockets and to model their time evolution and, in particular, their refilling with fresh magma and volatiles which is necessary for functioning of sustained generation of deep volcanic seismicity.

Data availability statement

This study makes no use of input data. The algorithm and its implementation for the 3-D modeling of quasi-static visco-elastic damage rheology are described in Lyakhovsky et al. (2001). The relevant details regarding the execution of model simulations are described in this manuscript. The fortran code used to carry out the calculations as well as the relevant input and output files together with the python scrip used for their visualization are available at the repository:
`https://zenodo.org/records/10409299` (DOI:10.5281/zenodo.10409299).

Acknowledgments
This study was supported by the European Research Council under the European Union Horizon 2020 research and innovation program (Grant Agreement 787399-SEISMAZE).

Appendix A Single bubble growth model

The process of a single bubble growth from a supersaturated magma is described by a set of Raleigh-Lamb equations together with diffusion equations for multiple dissolved volatiles:

$$\frac{\partial}{\partial r}\left(r^2\nu_r\right) = 0;\ \nu_r|_{r=R} = \frac{dR}{dt}; \tag{A1}$$

$$P_g - P_m = \frac{2\sigma}{R} + 4\mu\frac{dR}{dt}\left(\frac{1}{R} - \frac{R^2}{S^3}\right); \tag{A2}$$

$$P_m = P_m^0 + \frac{4}{3}G\left(\frac{S^3 - S_0^3}{S_0^3}\right); \tag{A3}$$

$$\frac{\partial c_s}{\partial t} + \nu_r\frac{\partial c_s}{\partial r} = \frac{1}{r^2}\frac{\partial}{\partial r}\left(D_s r^2\frac{\partial c_s}{\partial r}\right); \tag{A4}$$

$$\frac{4\pi}{3}\frac{d}{dt}\left(R^3\rho_g x_{CO2}^b\right) = 4\pi R^2 J_c; \tag{A5}$$

$$\frac{4\pi}{3}\frac{d}{dt}\left(R^3\rho_g\left(1 - x_{CO2}^b\right)\right) = 4\pi R^2 J_w; \tag{A6}$$

$$J_s = -D_c\rho_m\left(\frac{\partial c_c}{\partial r}\right)_{r=R};\ J_w = -D_w\rho_m\left(\frac{\partial c_w}{\partial r}\right)_{r=R}. \tag{A7}$$

$$\rho_g = \left(\frac{x^b_{CO2}}{\rho_{CO2}\left(P_g, T\right)} + \frac{1 - x^b_{CO2}}{\rho_{H2O}\left(P_g, T\right)} \right)^{-1}; \tag{A8}$$

$$\rho_{CO2} = (0.371 + 0.13 \times 10^{-3} T) P_g + 1194.65 - 0.4665T; \tag{A9}$$

$$\rho_{H2O} = (0.22 + 0.13 \times 10^{-3} T) P_g + 892.2 - 0.357T; \tag{A10}$$

$$D_w = c_{H2O} \exp\left(-8.56 - \frac{19110}{T}\right); \tag{A11}$$

$$D_c = \exp\left(-13.99 - \frac{(17367 + 1.945P_g)}{T} + \frac{c_{H2O}(855.2 + 0.271P_g)}{T}\right) \tag{A12}$$

Here t is time, r is the radial coordinate, R is the radius of the bubble, v_r is the radial velocity, index $s = w, c$ corresponds to water and carbon dioxide, respectfully, c_c and c_w are the mass concentrations of CO2 and H2O in the melt, D_c and D_w are the volatile diffusion coefficients, P_g is the pressure of the gas inside the bubble, P_m is the melt pressure, σ is the surface tension, μ is the magma viscosity, S is the radius of the cell, G is the shear modulus of the host rock, ρ_g is the density of the gas in the bubble that depends on the pressure, temperature T and bubble volatile composition x^b_{CO2}.

The densities of pure CO_2 and H_2O are approximated at a limited $P - T$ range using tables produced by NIST Chemistry WebBook (https://webbook.nist.gov/chemistry/).

Diffusion equations (A4) are subjected to two boundary conditions: concentration gradients are equal to zero at the outer surfaces of the cell mimicking symmetry of the system. At $r = R(t)$ volatiles in magma are in chemical equilibrium with the bubble. Thus, $c_s = c_s^{eq}\left(P_g, T, x^b_{CO2}\right)$.

The dynamics of bubble growth under various conditions have been widely discussed in the literature ((Gardner et al., 2023)). Based on the experimental observations we adopt that at the critical supersaturation for the bubble nucleation, the gas pressure, P_0, is several tens of MPa above the pressure of the surrounding melt. This initial pressure difference is compensated by the surface tension term (see equation A2), which decreases as 1/R. This surface tension decrease together with efficient volatile mass flux into the bubbles leads to a steep gas pressure increase. At the later stage the rate of the pressure growth decreases and gas pressure approaches to the equilibrium pressure, P_{eq}.

References

Aki, K., & Koyanagi, R. (1981). Deep volcanic tremor and magma ascent mechanism under kilauea, hawaii. *Journal of Geophysical Research: Solid Earth*, *86*(B8), 7095-7109. Retrieved from `https://agupubs.onlinelibrary.wiley.com/doi/abs/10.1029/JB086iB08p07095` doi: https://doi.org/10.1029/JB086iB08p07095

Aki, K., & Richards, P. G. (2002). *Quantitative seismology* (2nd ed.). University Science Books. Hardcover. Retrieved from `http://www.worldcat.org/isbn/0935702962`

Aso, N., Ohta, K., & Ide, S. (2013). Tectonic, volcanic, and semi-volcanic deep low-frequency earthquakes in western japan. *Tectonophysics*, *600*, 27-40. Retrieved from `https://www.sciencedirect.com/science/article/pii/S0040195112007949` (Great Earthquakes along Subduction Zones) doi: https://doi.org/10.1016/j.tecto.2012.12.015

Aso, N., & Tsai, V. C. (2014). Cooling magma model for deep volcanic long-period earthquakes. *J. Geophys. Res. Solid Earth*, *119*(11), 8442–8456. doi: 10.1002/2014JB011180

Ben-Menahem, A., & Singh, S. J. (2012). *Seismic waves and sources.* Springer Science & Business Media.

Bindeman, I. N., Melnik, O. E., Guillong, M., Utkin, I. S., Wotzlaw, J. F., Schmitt, A. K., & Stern, R. A. (2023). Age of the magma chamber and its physicochemical state under elbrus greater caucasus, russia using zircon petrochronology and modeling insights. *Scientific Reports*, *13*(1), 9733. Retrieved from `https://doi.org/10.1038/s41598-023-36793-y` doi: 10.1038/s41598-023-36793-y

Burgisser, A., Alletti, M., & Scaillet, B. (2015, Apr). *D-compress.* Retrieved from `https://theghub.org/resources/3791`

Cassidy, M., Manga, M., Cashman, K., & Bachmann, O. (2018). Controls on explosive-effusive volcanic eruption styles. *Nature Communications*, *9*(1), 2839. Retrieved from `https://doi.org/10.1038/s41467-018-05293-3` doi: 10.1038/s41467-018-05293-3

Chouet, B. (1986). Dynamics of a fluid-driven crack in three dimensions by the finite difference method. *Journal of Geophysical Research: Solid Earth*, *91*(B14), 13967-13992. Retrieved from `https://agupubs.onlinelibrary.wiley.com/doi/abs/10.1029/JB091iB14p13967` doi: https://doi.org/10.1029/JB091iB14p13967

Chouet, B., Dawson, P., & Arciniega-Ceballos, A. (2005). Source mechanism of vulcanian degassing at popocatépetl volcano, mexico, determined from waveform inversions of very long period signals. *Journal of Geophysical Research: Solid Earth*, *110*(B7). Retrieved from `https://agupubs.onlinelibrary.wiley.com/doi/abs/10.1029/2004JB003524` doi: https://doi.org/10.1029/2004JB003524

Chouet, B., Dawson, P., & Nakano, M. (2006). Dynamics of diffusive bubble growth and pressure recovery in a bubbly rhyolitic melt embedded in an elastic solid. *Journal of Geophysical Research: Solid Earth*, *111*(B7). Retrieved from `https://agupubs.onlinelibrary.wiley.com/doi/abs/10.1029/2005JB004174` doi: https://doi.org/10.1029/2005JB004174

Chouet, B. A. (1996). Long-period volcano seismicity: its source and use in eruption forecasting. *Nature*, *380*, 309-316. doi: 10.1038/380309a0

Cundall, P. A. (1988). Numerical experiments on localization in frictional materials. In *Proc. of the workshop on limit analysis and bifurcation theory.*

Fedotov, S. A., Zharinov, N. A., & Gontovaya, L. I. (2010). The magmatic system of the klyuchevskaya group of volcanoes inferred from data on its eruptions, earthquakes, deformation, and deep structure. *J. Volcanol. Geotherm. Res.*, *4*(1), 1–33. doi: 10.1134/S074204631001001X

Galina, N. A., Shapiro, N. M., Droznin, D. V., Droznina, S. Y., Senyukov, S. L., & Chebrov, D. V. (2020). Recurrence of deep long-period earthquakes beneath the Klyuchevskoi volcano group, Kamchatka. *Izvestiya, Physics of the Solid Earth*, *56*(6), 749–761. doi: 10.1134/S1069351320060026

Gardner, J. E., Wadsworth, F. B., Carley, T. L., Llewellin, E. W., Kusumaatmaja, H., & Sahagian, D. (2023). Bubble formation in magma. *Annual Review of Earth and Planetary Sciences*, *51*, 131–154. doi: https://doi.org/10.1146/annurev-earth-031621-080308

Greenfield, T., Winder, T., Rawlinson, N., Maclennan, J., White, R. S., Ágústsdóttir, T., ... Horálek, J. (2022). Deep long period seismicity preceding and during the 2021 fagradalsfjall eruption, iceland. *Bulletin of Volcanology*, *84*(12), 101. Retrieved from `https://doi.org/10.1007/s00445-022-01603-2` doi: 10.1007/s00445-022-01603-2

Hensch, M., Dahm, T., Ritter, J., Heimann, S., Schmidt, B., Stange, S., & Lehmann, K. (2019, 01). Deep low-frequency earthquakes reveal ongoing magmatic recharge beneath Laacher See Volcano (Eifel, Germany). *Geophysical Journal International*, *216*(3), 2025-2036. doi: 10.1093/gji/ggy532

Hess, K., & Dingwell, D. B. (1996). Viscosities of hydrous leucogranitic melts: A non-arrhenian model. *American Mineralogist: Journal of Earth and Planetary Materials*, *81*(9-10), 1297–1300.

Hirth, J., Pound, G., & St. Pierre, G. (1970). Bubble nucleation. *Metallurgical Transactions*, *1*, 939–945. doi: https://doi.org/10.1007/BF02811776

Ikegaya, T., & Yamamoto, M. (2021). Spatio-temporal characteristics and focal mechanisms of deep low-frequency earthquakes beneath the zao volcano, northeastern japan. *Journal of Volcanology and Geothermal Research*, *417*, 107321. Retrieved from https://www.sciencedirect.com/science/article/pii/S0377027321001505 doi: https://doi.org/10.1016/j.jvolgeores.2021.107321

Jaupart, C., & Vergniolle, S. (1988). Laboratory models of hawaiian and strombolian eruptions. *Nature*, *331*(6151), 58–60. Retrieved from https://doi.org/10.1038/331058a0 doi: 10.1038/331058a0

Journeau, C., Shapiro, L., N. M.and Seydoux, Soubestre, J., Koulakov, I. Y., Jakovlev, A. V., Abkadyrov, I., … Jaupart, C. (2022). Seismic tremor reveals active trans-crustal magmatic system beneath Kamchatka volcanoes. *Sci. Adv.*, *8*(5), eabj1571. doi: 10.1126/sciadv.abj1571

Koulakov, I., Shapiro, N. M., Sens-Schönfelder, C., Luehr, B. G., Gordeev, E. I., Jakovlev, A., … Stupina, T. (2020). Mantle and crustal sources of magmatic activity of Klyuchevskoy and surrounding volcanoes in Kamchatka inferred from earthquake tomography. *Journal of Geophysical Research: Solid Earth*, *125*(10), e2020JB020097. doi: 10.1029/2020JB020097

Kurihara, R., & Obara, K. (2021). Spatiotemporal characteristics of relocated deep low-frequency earthquakes beneath 52 volcanic regions in japan over an analysis period of 14 years and 9 months. *J. Geophys. Res. Solid Earth*, *126*(10), e2021JB022173. doi: 10.1029/2021JB022173

Kurihara, R., Obara, K., Takeo, A., & Tanaka, Y. (2019). Deep low-frequency earthquakes associated with the eruptions of shinmoe-dake in kirishimavolcanoes. *J. Geophys. Res. Solid Earth*, *124*(12), 13079-13095. doi: 10.1029/2019JB018032

Lensky, N. G., Niebo, R. W., Holloway, J. R., Lyakhovsky, V., & Navon, O. (2006). Bubble nucleation as a trigger for xenolith entrapment in mantle melts. *Earth and Planetary Science Letters*, *245*(1), 278-288. Retrieved from https://www.sciencedirect.com/science/article/pii/S0012821X06002135 doi: https://doi.org/10.1016/j.epsl.2005.11.064

Levin, V., Droznina, S. Y., Gavrilenko, M., Carr, M. J., & Senyukov, S. L. (2014). Seismically active subcrustal magma source of the klyuchevskoy volcano in kamchatka, russia. *Geol.*, *42*(11), 983-986. doi: 10.1130/G35972.1

Lu, L., & Bostock, M. G. (2022). Deep long-period earthquakes near mount meager, british columbia. *Canadian Journal of Earth Sciences*, *59*(7), 407-417. Retrieved from https://doi.org/10.1139/cjes-2021-0103 doi: 10.1139/cjes-2021-0103

Lyakhovsky, V., Ben-Zion, Y., Ilchev, A., & Mendecki, A. (2016). Dynamic rupture in a damage-breakage rheology model. *Geophysical Journal International*, *206*(2), 1126-1143. Retrieved from https://doi.org/10.1093/gji/ggw183 doi: 10.1093/gji/ggw183

Lyakhovsky, V., Hurwitz, S., & Navon, O. (1996). Bubble growth in rhyolitic melts: experimental and numerical investigation. *Bulletin of Volcanology*, *58*(1), 19–32. Retrieved from https://doi.org/10.1007/s004450050122 doi: 10.1007/s004450050122

Lyakhovsky, V., Ilchev, A., & Agnon. (2001). Modeling of damage and instabilities of rock mass by means of a non-linear rheological model. In G. Van Aswegen, R. J. Durrheim, & W. D. Ortlepp (Eds.), *Dynamic rock mass response to mining* (pp. 413–420). South African Institute of Mining and Metallurgy.

Maeda, Y., & Kumagai, H. (2017). A generalized equation for the resonance frequencies of a fluid-filled crack. *Geophysical Journal International*, *209*(1), 192–201. doi: 10.1093/gji/ggx019

Melnik, O., Lyakhovsky, V., Shapiro, N., Galina, N., & Bergal-Kuvikas, O. (2020). Deep long period volcanic earthquakes generated by degassing of volatile-rich basaltic magmas. *Nature Communications*, *11*(1), 3918. Retrieved from `https://doi.org/10.1038/s41467-020-17759-4` doi: 10.1038/s41467-020-17759-4

Melnik, O. E., Utkin, I. S., & Bindeman, I. N. (2021). Magma chamber formation by dike accretion and crustal melting: 2d thermo-compositional model with emphasis on eruptions and implication for zircon records. *Journal of Geophysical Research: Solid Earth*, *126*(12), e2021JB023008. Retrieved from `https://agupubs.onlinelibrary.wiley.com/doi/abs/10.1029/2021JB023008` (e2021JB023008 2021JB023008) doi: https://doi.org/10.1029/2021JB023008

Mironov, N., & Portnyagin, M. (2011). H2o and co2 in parental magmas of kliuchevskoi volcano inferred from study of melt and fluid inclusions in olivine. *Russian Geology and Geophysics*, *52*(11), 1353-1367. Retrieved from `https://www.sciencedirect.com/science/article/pii/S1068797111002161` (Melts and Fluids in Natural Mineral and Ore Formation Processes: Modern Studies of Fluid and Melt Inclusions in Minerals) doi: https://doi.org/10.1016/j.rgg.2011.10.007

Nichols, M., Malone, S., Moran, S., Thelen, W., & Vidale, J. (2011). Deep long-period earthquakes beneath washington and oregon volcanoes. *J. Volcanol. Geotherm. Res.*, *200*(3), 116-128. doi: 10.1016/j.jvolgeores.2010.12.005

Nishimura, T. (2004). Pressure recovery in magma due to bubble growth. *Geophysical Research Letters*, *31*(12). Retrieved from `https://agupubs.onlinelibrary.wiley.com/doi/abs/10.1029/2004GL019810` doi: https://doi.org/10.1029/2004GL019810

Papale, P. (1999). Modeling of the solubility of a two-component h2o+ co2 fluid in silicate liquids. *American Mineralogist*, *84*(4), 477–492. doi: https://doi.org/10.2138/am-1999-0402

Pitt, A. M., & Hill, D. P. (1994). Long-period earthquakes in the long valley caldera region, eastern california. *Geophysical Research Letters*, *21*(16), 1679-1682. Retrieved from `https://agupubs.onlinelibrary.wiley.com/doi/abs/10.1029/94GL01371` doi: https://doi.org/10.1029/94GL01371

Poliakov, A. N. B., Cundall, P. A., Podladchikov, Y. Y., & Lyakhovsky, V. A. (1993). An explicit inertial method for the simulation of viscoelastic flow: an evaluation of elastic effects on diapiric flow in two-and three-layers models. In *Flow and creep in the solar system: observations, modeling and theory* (pp. 175–195). Springer.

Portnyagin, M., Hoernle, K., Plechov, P., Mironov, N., & Khubunaya, S. (2007). Constraints on mantle melting and composition and nature of slab components in volcanic arcs from volatiles (h2o, s, cl, f) and trace elements in melt inclusions from the kamchatka arc. *Earth and Planetary Science Letters*, *255*(1), 53-69. Retrieved from `https://www.sciencedirect.com/science/article/pii/S0012821X06008727` doi: https://doi.org/10.1016/j.epsl.2006.12.005

Portnyagin, M., Mironov, N., Botcharnikov, R., Gurenko, A., Almeev, R. R., Luft, C., & Holtz, F. (2019). Dehydration of melt inclusions in olivine and implications for the origin of silica-undersaturated island-arc melts. *Earth and Planetary Science Letters*, *517*, 95-105. Retrieved from `https://www.sciencedirect.com/science/article/pii/S0012821X19302250` doi: https://doi.org/10.1016/j.epsl.2019.04.021

Power, J., Stihler, S., White, R., & Moran, S. (2004). Observations of deep long-period (dlp) seismic events beneath aleutian arc volcanoes; 1989–2002. *J. Volcanol. Geotherm. Res*, *138*(3), 243–266. doi: 10.1016/j.jvolgeores.2004.07.005

Shapiro, N. M., Droznin, D. V., Droznina, S. Y., Senyukov, S. L., Gusev, A. A.,

& Gordeev, E. I. (2017). Deep and shallow long-period volcanic seismicity linked by fluid-pressure transfer. *Nat. Geosci.*, *10*(6), 442–445. doi: 10.1038/ngeo2952

Shapiro, N. M., Sens-Schönfelder, C., Lühr, B. G., Weber, M., Abkadyrov, I., Gordeev, E. I., . . . Saltykov, V. A. (2017). Understanding kamchatka's extraordinary volcano cluster. *Eos*, *98*. doi: 10.1029/2017EO071351

Shea, T. (2017). Bubble nucleation in magmas: a dominantly heterogeneous process? *Journal of Volcanology and Geothermal Research*, *343*, 155–170. doi: https://doi.org/10.1016/j.jvolgeores.2017.06.025

Song, Z., Tan, Y. J., & Roman, D. C. (2023). Deep long-period earthquakes at akutan volcano from 2005 to 2017 better track magma influxes compared to volcano-tectonic earthquakes. *Geophysical Research Letters*, *50*(10), e2022GL101987. Retrieved from `https://agupubs.onlinelibrary.wiley.com/doi/abs/10.1029/2022GL101987` (e2022GL101987 2022GL101987) doi: https://doi.org/10.1029/2022GL101987

Soubestre, J., Seydoux, L., Shapiro, N. M., de Rosny, J., Droznin, D. V., Droznina, S. Y., . . . Gordeev, E. I. (2019). Depth migration of seismovolcanic tremor sources below the klyuchevskoy volcanic group (kamchatka) determined from a network-based analysis. *Geophysical Research Letters*, *46*(14), 8018-8030. Retrieved from `https://agupubs.onlinelibrary.wiley.com/doi/abs/10.1029/2019GL083465` doi: https://doi.org/10.1029/2019GL083465

Sparks, R. S. J. (1978). The dynamics of bubble formation and growth in magmas: a review and analysis. *Journal of Volcanology and Geothermal Research*, *3*(1-2), 1–37. doi: https://doi.org/10.1016/0377-0273(78)90002-1

Ukawa, M., & Ohtake, M. (1987). A monochromatic earthquake suggesting deep-seated magmatic activity beneath the izu-ooshima volcano, japan. *J. Geophys. Res. Solid Earth*, *92*(B12), 12649-12663. doi: 10.1029/JB092iB12p12649

Wallace, P. J., Plank, T., Edmonds, M., & Hauri, E. H. (2015). Chapter 7 - volatiles in magmas. In H. Sigurdsson (Ed.), *The encyclopedia of volcanoes (second edition)* (Second Edition ed., p. 163-183). Amsterdam: Academic Press. Retrieved from `https://www.sciencedirect.com/science/article/pii/B9780123859389000079` doi: https://doi.org/10.1016/B978-0-12-385938-9.00007-9

Wech, A. G., Thelen, W. A., & Thomas, A. M. (2020). Deep long-period earthquakes generated by second boiling beneath mauna kea volcano. *Science*, *368*(6492), 775-779. doi: 10.1126/science.aba4798

White, R. A., Newhall, C. G., & Punongbayan, R. S. (1996). Precursory deep long-period earthquakes at mount pinatubo: Spatio-temporal link to a basalt trigger. *Fire and mud: Eruptions and lahars of Mount Pinatubo, Philippines*, 307–328.

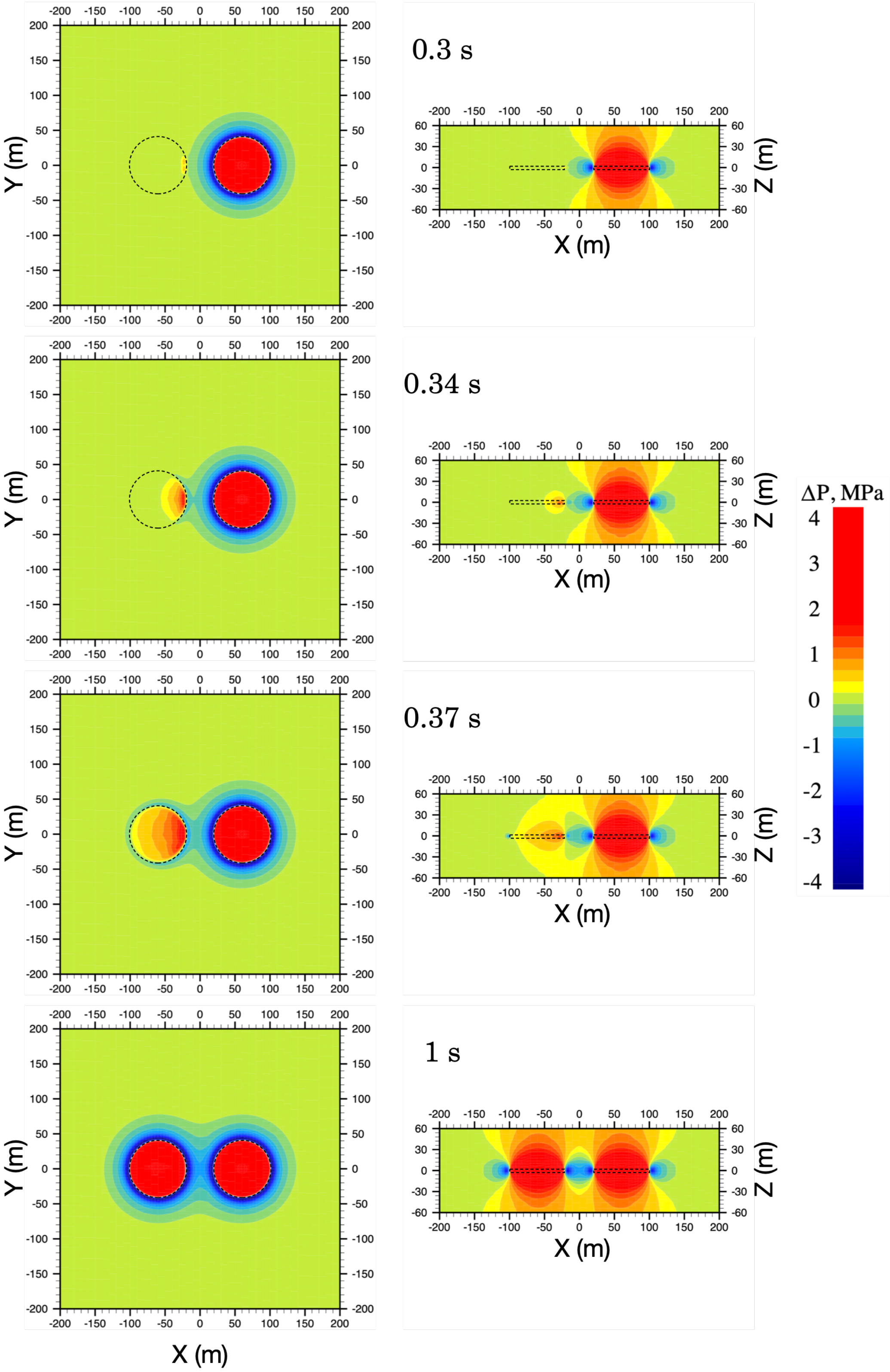

Figure 8. Snapshots of pressure evolution in time in a model with two interacting sills (distance 120 m, model N4-1). Left and right frames show horizontal and vertical cross-sections at Z=0 and Y=0, respectively. Times are indicated above the frames. Dashed lines indicate the boundaries of the magmatic sill.

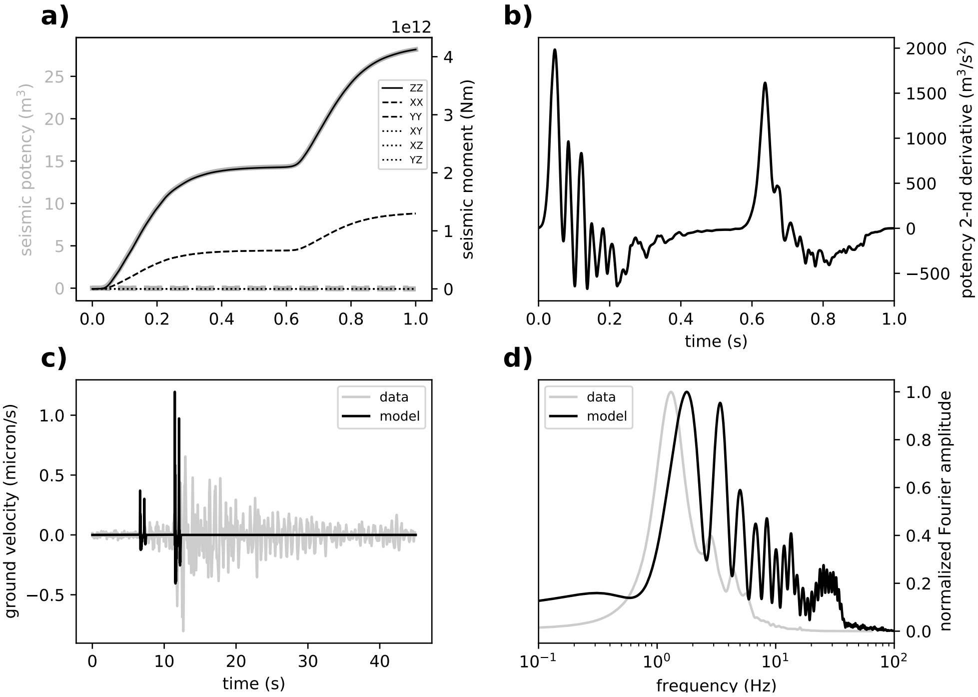

Figure 9. Similar to Figure 5 but model N4-2.

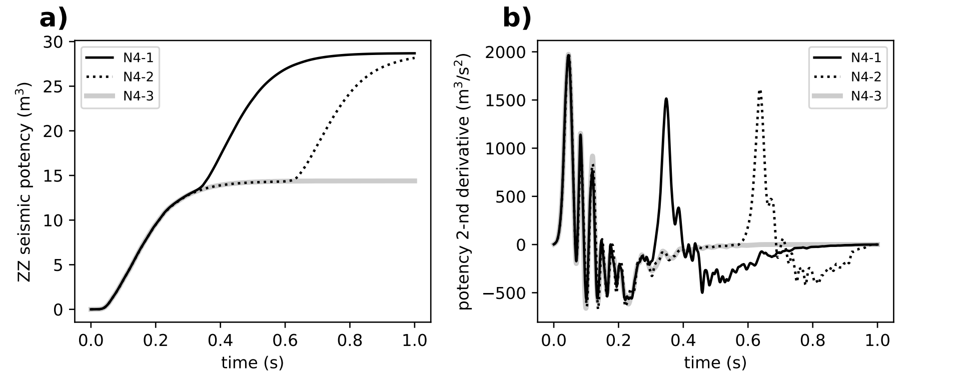

Figure 10. Comparison of seismic source time functions for models with two sills. (a) ZZ components of the seismic potency tensors as function of time. (b) Second derivatives of the ZZ potency function.

Rapid degassing in basaltic sills as a source of Deep Long Period volcanic earthquakes

Oleg Melnik[1],**Vladimir Lyakhovsky**[2], **Nikolai M. Shapiro**[1]

[1]ISTerre, Université Grenoble Alpes, CNRS, Université Savoie Mont Blanc, IRD, Université Gustave Eiffel, Grenoble, France
[2]Geological Survey of Israel, Jerusalem, Israel

Key Points:

- Spontaneous bubble nucleation leads to rapid pressure increase in a batch of magma.
- Bubble nucleation in the center of a sill filled with magma results in a propagation of a nucleation front inside the sill.
- Expanding sill generate P and S seismic waves with amplitudes and frequencies close to the observations.

Corresponding author: Nikolai Shapiro, `Nikolai.Shapiro@univ-grenoble-alpes.fr`

Abstract

In this paper, we present numerical modeling aimed to explain Deep Long Period (DLP) events occurring in middle-to-lower crust beneath volcanoes and often observed in association with volcanic eruptions or their precursors. We consider a DLP generating mechanism caused by the rapid growth of gas bubbles in response to the slow decompression of H_2O–CO_2 over-saturated magma. The nucleation and rapid growth of gas bubbles lead to rapid pressure change in the magma and elastic rebound of the host rocks, radiating seismic waves recorded as DLP events. The magma and host rocks are modeled as Maxwell bodies with different relaxation times and elastic moduli. Simulations of a single sill-shaped intrusion with different parameters demonstrate that realistic amplitudes and frequencies of P and S seismic waves can be obtained when considering intrusions with linear sizes of the order of 100 m. We then consider a case of two closely located sills and model their interaction. We speculate on conditions that can result in consecutive triggering of the bubble growth in multiple closely located batches of magma, leading to the generation of earthquake swarms or seismic tremors.

1 Plain Language Summary

Volcano seismology is one of the main geophysical methods used to study volcanic processes and to forecast the eruptions. It is based on analysis of ground motion recorded by seismographs installed in the vicinity of volcanoes. Different seismic signals such as impulsive volcanic earthquakes and nearly continuous volcanic tremors are recorded during periods corresponding to preparation of eruptions. Some of them originate from depths of a few tens of kilometers, i.e., from the roots of the system that feeds the magma supply to volcanoes and their eruptions. Therefore, such deep seismic sources are particularly interesting because they may represent early eruption precursors. While we still lack physical understanding of the processes leading to this deep volcanic seismicity, there are several reasons to consider that it is not caused by a sudden slip on faults responsible for the majority of "regular tectonic" earthquakes. In this paper, we use numerical simulations to test another possible mechanism of generation of deep volcanic earthquakes. Namely, we assume that they can be caused by rapid growth of bubbles from the gas that was initially dissolved in the magma. We use numerical simulations to demonstrate that this model predicts main properties of the observed seismic signals.

2 Introduction

Degassing is one of the main driving forces behind the volcanic activity. The separation of gas and melt phases leads to the formation of bubbles, whose presence increases the magma buoyancy thereby leading to its ascent. Degassing is very strong at the very top part of volcanic systems where most of gases, especially H_2O, no longer remain dissolved due to the pressure decrease (e.g., Wallace et al., 2015). Therefore, dynamics of gas bubbles in the magma is predominant during the eruptions (e.g., Jaupart & Vergniolle, 1988; Cassidy et al., 2018) and other near-surface volcano-related processes. In particular, the degassing and associated bubble growth can cause significant magma pressure variations. If these pressure perturbations are sufficiently rapid, they are transmitted into the surrounding elastic media as seismic waves that can be recorded by seismographs as volcanic earthquakes. Such rapid pressure changes can occur when a magma volume first reaches the saturation level and then achieves the critical supersaturation after which the gas bubbles nucleate and grow rapidly (Lyakhovsky et al., 1996; Lensky et al., 2006).

In one scenario, a rapid decompression of a shallow intrusion caused by a sudden gas escape via conduit results in a critical magma supersaturation. This pressure drop is fallowed by a pressure recovery because of the gas bubble grows (Nishimura, 2004). B. Chouet et al. (2006) modeled such sequence of magma depressurisation-pressurisation and related elastic deformation of the surrounding rocks in order to explain very long period seismic signals associated with the Vulcanian explosions at Popocatépetl Volcano in Mexico (B. Chouet et al., 2005). They considered a sill-shaped volume of rhyolitic magma at a depth of 1.5 km. The system response has been found to depend strongly on various parameters such as volatile diffusivity in the melt, the bubble number density, the initial bubble radius, and the shape of the intrusion. The model could reasonably explain observed seismic waveforms within the range of acceptable parameters and predicted pressure variations of the order of a few MPa with characteristic timescale of tens of seconds.

Another scenario has been recently considered by O. Melnik et al. (2020) to explain the Deep Long Period (DLP) earthquakes occurring in middle-to-lower crust beneath volcanoes and often associated with eruptions or their precursors (e.g., Ukawa & Ohtake, 1987; Pitt & Hill, 1994; White et al., 1996; Power et al., 2004; Nichols et al., 2011; Aso et al., 2013; Aso & Tsai, 2014; Shapiro, Droznin, et al., 2017; Hensch et al., 2019; Kurihara et al., 2019; Wech et al., 2020; Ikegaya & Yamamoto, 2021; Kurihara & Obara, 2021; Greenfield et al., 2022; Lu & Bostock, 2022; Song et al., 2023). In some cases, the origin of these DLP earthquakes has been attributed to the processes occurring within a cooling magma body stalled beneath the crust such thermal stresses (Aso et al., 2013) or "second boiling", i.e., repeated pressurization by volatiles exsolution during magma crystallization (Wech et al., 2020). However, such cooling-related mechanisms are unlikely for DLP events occurring beneath active volcanoes in association with eruptions. Therefore, O. Melnik et al. (2020) suggested a possible DLP generating mechanism related to the rapid growth of gas bubbles in response to the slow decompression of oversaturated magma. In this model, a volume of magma saturated with H_2O–CO_2 volatiles is slowly rising up which causes its depressurisation. This magma first reaches the saturation level and then achieves the critical supersaturation after which gas bubbles nucleation causes rapid pressure and elastic stress variations resulting in seismic waves recorded as DLP earthquakes.

The model of O. Melnik et al. (2020) was particularly aimed to explain the DLP earthquakes occurring beneath the Klyuchevskoy volcano in Kamchatka, Russia (e.g., Fedotov et al., 2010; Shapiro, Sens-Schönfelder, et al., 2017; Koulakov et al., 2020) just beneath the crust-mantle boundary (Levin et al., 2014; Shapiro, Droznin, et al., 2017; Galina et al., 2020; Journeau et al., 2022) at a depth of approximately 30-35 km. Recent studies suggested that primary Klyichevskoy magma may contain more than 4 wt% H_2O and 0.35–0.9 wt% CO_2 (Portnyagin et al., 2007; Mironov & Portnyagin, 2011; Portnyagin et al., 2019). Single H_2O volatile phase would result in a small saturation depth, but the addition of 0.6 wt% of CO_2decreases volatile solubility dramatically (Papale, 1999; Burgisser et al., 2015) so that magma becomes super-saturated at pressures of above 800 MPa (30 km depth).

O. Melnik et al. (2020) have shown that for realistic magma compositions and values of the gas and bubble content, the elastic deformation of surrounding rocks forced by the expanding bubbly magma can be fast enough to generate seismic waves. They approximately estimated a volume of degassing magma of $\sim 10^3 - 10^4 m^3$ would be necessary to explain amplitudes of signals recorded from the DLP earthquakes beneath the Klyuchevskoy volcano. Nevertheless, this model contained important approximations. First, an instantaneous bubble nucleation in the whole batch of magma was assumed, similar to B. Chouet et al. (2006). However, such scenario is unlikely within the slowly uplifting magma batch. In this case, we can rather expect that the babble growth will be first triggered in a small volume and than spontaneously propagate through the rest of the magma body. Second limitation of O. Melnik et al. (2020) was that only a spherical-shape intrusion was modeled. Also, excitation of seismic waves was not explicitly computed and the amplitudes of seismograms were predicted based on a simplified approximation.

To overcome the mentioned shortcomings, we developed a more complete and accurate model of generation of seismic waves by the pressure variations caused by bubbles growth in magma. The model is based on an accurate numerical solution of coupled fluid-elastic equations and includes: (1) a bubble nucleation front propagating from initial trigger point, (2) a sill-shape magma intrusion, and (3) an exact estimation of the associated seismic potency (moment) tensor in order to compute the seismograms.

We start with formulating the mechanical model in section 3. A particular attention is payed to an accurate description of the compressibility of the bubbly magma and its variations in association with the bubble growth. We then apply the developed mechanical framework to model the gas bubble growth in an intrusion shaped as a horizontal sill. The numerical implementation and model settings are described in section 4. The results of the modeling are presented in section 5 and their implications are discussed in section 6. In particular, after considering solutions for a single sill-shaped intrusion with different parameters, we introduce a case of two closely located sills and model their interaction. We then speculate how such interaction can result in consecutive triggering of the bubble growth in multiple closely located intrusions and lead to generation of earthquake swarms or seismic tremors.

3 Mechanical model of a DLP earthquake source

3.1 Conceptual model

We consider a scenario illustrated in Figure 1a. Basaltic magmas rising from the mantle are underplated beneath the Moho forming sill-shaped intrusions. Following O. Melnik et al. (2020), we consider that H_2O-CO_2 rich basaltic magma becomes oversaturated at these depths leading to a spontaneous nucleation and rapid growth of gas bubbles within the sill (Figure 1b). Magma degassing in an initial small volume leads to perturbations of the pressure in its vicinity that, in turn, results in nucleation and growth of new bubbles. Such "nucleation" front propagates along the whole sill (Figure 1c) causing it expansion (Figure 1d) and leading to elastic deformation of the surrounding rocks and generation of seismic waves that are then recorded by seismographs installed at the surface.

3.2 Mathematical formulation for a coupled fluid-solid system with bubbles

The mechanical model for the scenario described above consists of a sill-shaped cavity filled with a viscous fluid (magma) embedded in an elastic medium (rocks). We solve the equations of motion for a continuum media in the whole volume of the model without body force:

$$\rho \frac{\partial^2 u_i}{\partial t^2} = \frac{\partial \sigma_{ij}}{\partial x_j} \tag{1}$$

where ρ – material density; u_i – displacement vector; σ_{ij} – stress tensor. The total strain is calculated from the displacement field as:

$$\varepsilon_{ij}^t = \frac{1}{2}\left(\frac{\partial u_i}{\partial x_j} + \frac{\partial u_j}{\partial x_i}\right) \tag{2}$$

Different stress–strain constitutive relations (different rheology) are adopted for the magma and the surrounding material. The host rock is simulated as perfectly elastic isotropic Hookean solid ($\varepsilon^t = \varepsilon^e$, where index e corresponds to elastic deformations). The constitutive stress-strain relations for elastic deformations are:

$$\sigma_{ij} = \lambda \varepsilon_{kk}^e \delta_{ij} + 2\mu \varepsilon_{ij}^e \tag{3}$$

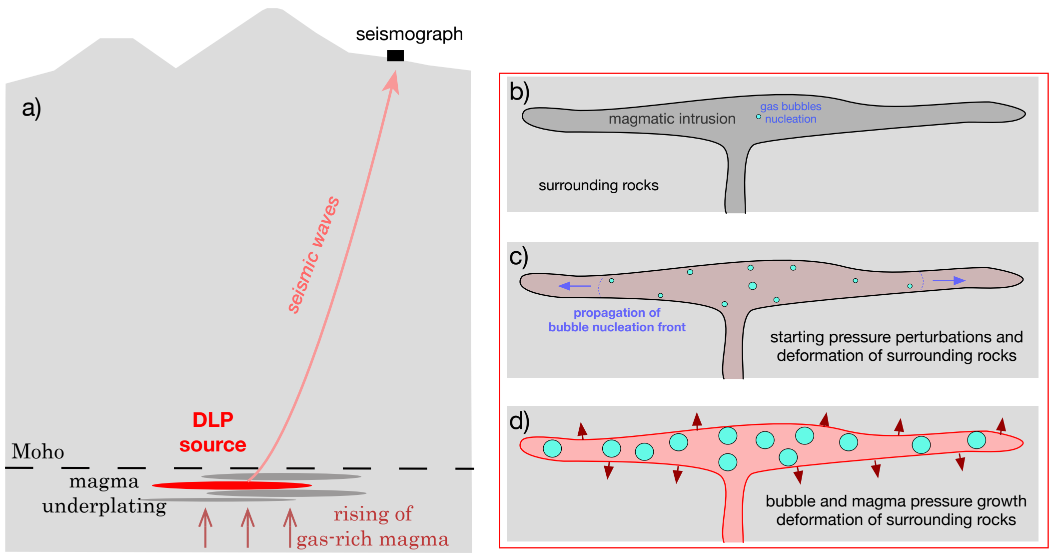

Figure 1. Schematic representation of the DLP source model. (a) General geometry with a source (a sill filled with a rapidly degassing magma highlighted with the red color) located at the crust-mantle boundary and the station recording seismic waves located at the surface. (b)-(d) Main stages of the rapid degassing of the magma within a sill.

where λ and μ are Lame elastic modulus.

Magma is approximated by Maxwell visco-elastic body with the total strain, ε_{ij}^{t}, being a sum of the elastic, ε_{ij}^{e} and irreversible, ε_{ij}^{irr}, strain components.

$$\varepsilon_{ij}^{t} = \varepsilon_{ij}^{e} + \varepsilon_{ij}^{irr}, \tag{4}$$

Adopting the Newtonian stress – strain-rate relations for a viscous fluid, the deviatoric stress, $\tau_{ij} = \sigma_{ij} + P\delta_{ij}$ (where $P = -trace(\sigma_{ij})/3$ is the pressure) we obtain:

$$\tau_{ij} = \eta \frac{\partial \varepsilon_{ij}^{irr}}{\partial t}, \qquad \varepsilon_v = P/K \tag{5}$$

where η is the melt viscosity. The volumetric strain component ε_v for the bubble-free magma is calculated using the magma compressibility K. The magma remains bubble-free until the pressure is above the critical value associated with super-saturation of the gas dissolved in the melt.

As soon as the critical magma super-saturation is reached, bubbles nucleate and start to expand. The dynamics of bubble growth under various conditions have been widely discussed in the literature (see reviews by (Sparks, 1978; Gardner et al., 2023) and references therein). According to the bubble growth model (Lyakhovsky et al., 1996) the gas diffusion into the small bubble is very efficient at the initial stage of growth following the nucleation. The initial pressure difference or nucleation pressure is partly compensated by the surface tension term, which decreases as inverse of the bubble radius, $1/R$. The surface tension steeply decreases with the bubble growth and the pressure driving the bubble expansion practically remains constant. At this stage, the exponential increase of the bubble radius is controlled by the viscosity of the surrounding melt and the nucleation over-pressure $\Delta P = P_s - P_0$ or the difference between the saturation pressure, P_s, and the pressure in the surrounding melt, P_0. With the increase of the bubble radius, the efficiently of the diffusion decreases, and the rate of the bubble growth is controlled by the diffusive gas flux from the surrounding melt cell with a radius S. Finally, the bubble size and gas pressure approach their equilibrium values depending on the initial values of pressure, gas concentration, and cell size, as well as melt properties. The initial cell size, S_0, or the melt volume surrounding every bubble may be calculated assuming certain number of bubbles nucleated from the unit melt volume, or bubble number density, N_d:

$$\frac{4}{3}\pi S_0^3 = \frac{1}{N_d} \tag{6}$$

The details of a single bubble growth model developed by (O. Melnik et al., 2020) consists of Raleigh-Lamb equation coupled with diffusion equations for multiple dissolved volatile and is briefly discussed in Appendix Appendix A.

The pressure inside the bubble P_g just after nucleation is equal to the saturation pressure P_s. It is several tens of MPa higher than the initial pressure in the surrounding melt P_0. At final stage of the bubble growth both gas and melt P_m pressures approaches to the equilibrium pressure, P_{eq}. We can define the pressure in the bubbly magma P_b as:

$$P_b = P_g\alpha + P_m(1-\alpha), \tag{7}$$

where α is the volume fraction of bubbles, $\alpha = \frac{R^3}{S_0^3}$.

Figure 2 shows the overpressure, $P_b - P_0$, evolution in the bubbly magma pocket simulated by the model from O. Melnik et al. (2020) for three different values of the bubble number densities, $N_d = 10^{13}/m^3$ (green line), $N_d = 10^{14}/m^3$ (red line), $N_d = 10^{15}/m^3$ (blue line). Here we use the initial over-pressure of $\Delta P = P_s - P_0 = 40$ MPa (Shea, 2017). This pressure increase leads to a deformation of the surrounding rock mass and serves as a source pressure for the sill opening. The S-shape of the pressure curves could be well approximated by an exponential function:

$$P_b = P_{eq} - (P_{eq} - P_0) * exp(b * \delta t^{\gamma}) \tag{8}$$

where δt is time since the bubble nucleation; $\gamma = 2.4$. The fitting coefficient b significantly depends on the assumed bubble number density. The fitted values are: $b = -28$ for $N_d = 10^{13}/m^3$, $b = -187$ for $N_d = 10^{14}/m^3$, and $b = -1355$ for $N_d = 10^{15}/m^3$. Figure 2 shows the comparison between calculated and fitted pressure variations for different number density of bubbles.

The equilibrium pressure in the melt pocket depends on the deformation of the surrounding rock and volume change of the considered bubbly melt pocket. It is calculated using the mass conservation law of the gas, stored in the bubble and dissolved in the surrounding melt, $m_g = Const.$:

$$m_g = \frac{4}{3}\pi S_0^3 C\rho_m + \frac{4}{3}\pi R^3\rho_g = \frac{4}{3}\pi S_0^3 C_s\rho_m \tag{9}$$

where C_s is the gas concentration at the super-saturation needed for the bubble nucleation, ρ_m is the melt density. We use linear approximation for gas density, ρ_g:

$$\rho_g = a_r(P - P_0) + b_r \tag{10}$$

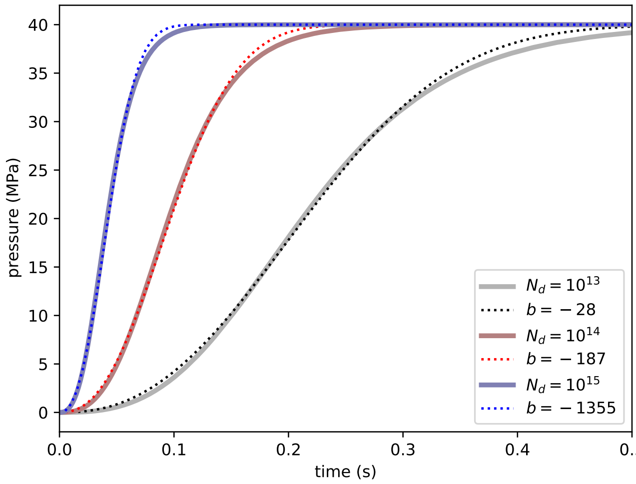

Figure 2. Comparison between calculated and fitted pressure variations for different number density of bubbles

and solubility, C:

$$C = a_c(P - P_0) + C_0 \tag{11}$$

with the following values: $a_c = 1.4410^{-5}/MPa$, $a_r = 0.586kg/m^3/MPa$ $b_r = 419.0kg/m^3$. The value of C_0 defines the volatile concentration at pressure P_0.

Substituting these linear approximation into the gas mass balance equation (9)

$$S_0^3\rho_m\left(a_c(P_{eq} - P_0) + C_0\right) + R^3\left(a_r(P_{eq} - P_0) + b_r\right) = S_0^3\rho_m(a_c(P_s - P_0) + C_0) \tag{12}$$

and dividing by S_0^3 leads to:

$$\rho_m\left(a_c(P_{eq} - P_0) + C_0\right) + \alpha\left(a_r(P_{eq} - P_0) + b_r\right) = \rho_m(a_c(P_s - P_0) + C_0) \tag{13}$$

By solving equation (13) against P_{eq} we obtain the relation that adjusts equilibrium pressure in equation (8)

$$P_{eq} = \frac{\rho_m a_c P_s + \alpha(a_r P_0 - b_r)}{\alpha a_r + a_c\rho_m} \tag{14}$$

Equation (8) together with (14) govern the evolution of the source pressure in the bubbly magma. As soon as the nucleation condition is reached in particular cell instead of using equation (5) to calculate the pressure from volumetric strain, we assume that the pressure is specified by equation (8) and the volume fraction of bubbles is calculated as a difference between the total volume change and the elastic melt expansion:

$$\alpha = \varepsilon_v - P_b/K; \tag{15}$$

The equilibrium pressure is then calculated from equation (14). Obtained P_{eq} and re-calculated P_b values are used for the time marching.

If this deformation is sufficiently rapid, the seismic waves are transmitted into the surrounding elastic media and recorded by seismographs as volcanic earthquakes. The earthquake source mechanism is estimated by integrating the irreversible strain over the sill volume:

$$\Pi_{ij}(t) = \int_V \varepsilon_{ij}^{irr}(t) d^3x \tag{16}$$

Following Ben-Menahem and Singh (2012) this tensor is called potency or geometrical moment. The time-dependent moment tensor components are calculated using the Hook stress-strain relations with Lame parameters λ and μ of the host rock:

$$M_{ij}(t) = \lambda \Pi_{kk} \delta_{ij} + 2\mu \Pi_{ij} \tag{17}$$

Synthetic seismograms are then computed as a convolution of the time-dependent seismic moment with the Green's function. For the latter we use the far-field P and S waves in a homogeneous elastic media (Aki & Richards, 2002). The near-field terms of the Green's function are ignored because the source-receiver distance is significantly larger than the wavelengths at dominant frequencies (above 1 Hz).

4 Numerical method and model settings

The 3D numerical modeling was performed using Explicit Finite Difference Lagrangian method, based on the FLAC (Fast Lagrangian Analyze of Continua) algorithm originally developed by Cundall (1988) for elasto-plastic rheology and implemented in the ITASCA software. The FLAC algorithm was modified for visco-elastic media (Poliakov et al., 1993). A modified version of this code incorporating heat transport is known as PAROVOZ and is widely used by many researchers. Lyakhovsky et al. (2001) developed their own 3-D code for quasi-static visco-elastic damage rheology modelling, which was used in many geodynamic applications. Later on the code was modified for dynamic processes, by reducing force damping to realistic values corresponding to wave attenuation. The numerical time-step was defined according to the Courant–Friedrichs–Lewy stability condition for explicit time-marching simulations. Technical details of the numerical approach for dynamic modelling of seismic wave propagation were discussed by Lyakhovsky et al. (2016).

We considered several cases of the model geometry. Most of simulations were performed for the model volume 200x200x100 m with a 50 m radius and 3 m thick penny-shaped sill located in the center (Figure 3a). In a few cases the model size have been doubled (both model dimensions and sill radius) keeping the same thickness. In the last series of the model runs two penny-shaped sills with 40 meter radius located in the same plain with three different distances, 40, 45, 50 m., between their edges (Figure 3b). The adaptive grid with tetrahedral elements with 0.5 meter grid step represents the sill volume. The grid size gradually increases in vertical direction away from the sill.

Equation (1) is solved with fixed zero displacement boundaries with attached narrow layer of highly damping material that prohibits the reflection of waves traveling inside the host rock. The initial stress is equal to the solubility pressure P_0 and zero deviatoric components.

The elastic material surrounding the sill has the properties close to those of the mantle: the density $\rho = 3000\, kg/cm^3$, bulk modulus K of 80 GPa, and rigidity (shear modulus) μ of 50 GPa. With these properties the seismic wave velocities in the host rock are: V_p=7 km/s, V_s=4.1 km/s. The density of the melt inside the sill is $\rho_m = 2800\, kg/cm^3$,

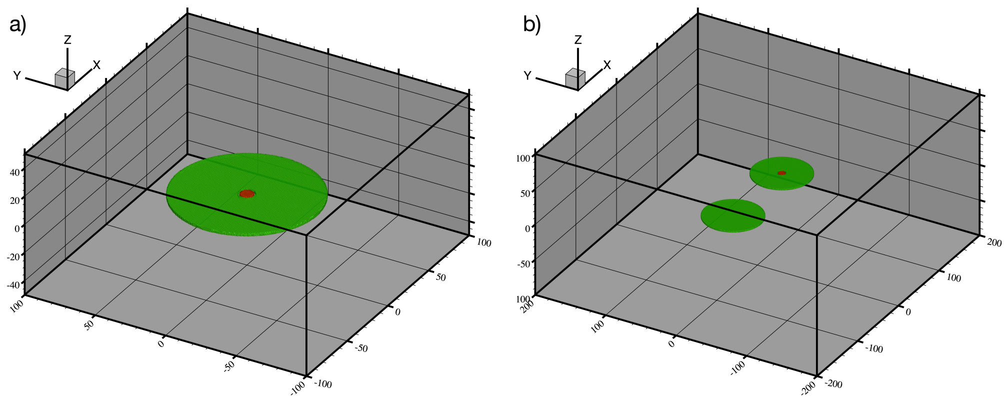

Figure 3. Geometries used in numerical simulations. (a) A penny-shaped sill of 50 m radius and 1 m thickness. Red color show the volume in which the bubble grow is triggered. (b) Two penny-shaped sill of 40 m radius and 1 m thickness. The bubble growth is triggered in the center one of the sills as shown with red color.

bulk modulus 10 GPa, and very low rigidity (5 orders of magnitude below the host rock rigidity). Melt viscosity (η) varied between 10 and 10^3 Pa*s between different model runs. These values provide numerical stability of the Maxwellian visco-elastic solution with negligibly small elastic shear strain components in the melt. The shear stress in the melt is controlled by the product of the strain rate and melt viscosity, like in the Newtonian fluid. For the small volume fraction of bubbles the magma viscosity variations due to bubble content might be neglected. During the simulation the event potency is calculated by integrating the inelastic strain over the volume of the sill (equation 16).

After estimating the potency tensor, we compute the propagation of seismic waves through the crust with average density of 2900 kg/m^3 and P and A wave velocities of 6062 and 3500 m/s, respectively. We consider a source-receiver distance of 40 km and a take-off angle at the source of 30°. This approximates the geometry with a curved seismic ray reaching a station located nearly above the source.

5 Results

During the study we considered fifteen different models (see Table 1), twelve of them for a single sill (Figure 3a) and the last three for two discs (Figure 3b). All the simulations start with a spontaneous bubble nucleation in the 5 meter circle area located in the center of the sill (red zone in Figure 3). In the case of a non-deformable surrounding material and adopted melt parameters the maximal over-pressure may grow up to about 40 MPa in respect of the initial pressure P_0. However, its final value is significantly reduced because of the elastic deformation of the surrounding rock and the increase of the sill volume (see equation (14).

5.1 Single sill configuration

Figure 4 shows four horizontal and vertical cross sections for sequential snapshots of pressure evolution for model N1-B (see Table 1 for parameters). Dashed lines on each cross section indicate the boundaries of the magmatic sill, where the bubble nucleation is expected.

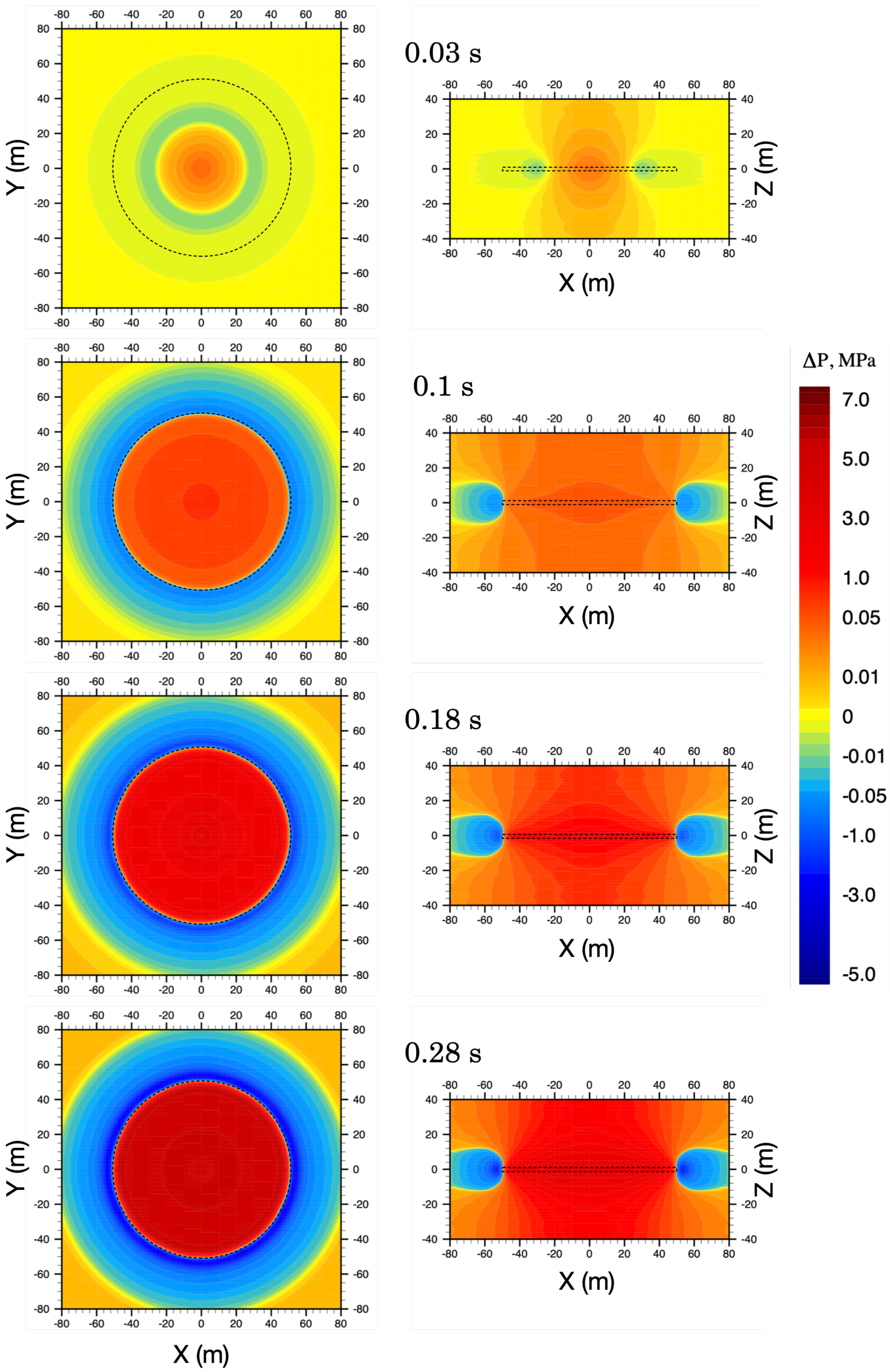

Figure 4. Snapshots of pressure evolution in time in a model N1-B. Left and right frames show horizontal and vertical cross-sections at Z=0 and Y=0, respectively. Time is indicated above the frames.

Run #	**Model ID**	**Sill size m**	**Nd $1/m^3$**	**Nucleation threshold, kPa**	**Melt viscosity Pa s**	**Potency m^3**
1	N1 A	50	10^{13}	10	100	22.325
2	N1 B	50	10^{13}	30	100	21.692
3	N1 C	50	10^{13}	50	100	20.238
4	N2 A	50	10^{14}	10	100	22.286
5	N2 B	50	10^{14}	30	100	22.133
6	N2 C	50	10^{14}	50	100	21.895
7	N3 A	50	10^{15}	10	100	22.121
8	N3 B	50	10^{15}	30	100	21.875
9	N3 C	50	10^{15}	50	100	21.651
10	N1 B V01	50	10^{13}	30	10	22.300
11	N1 B V10	50	10^{13}	30	1,000	22.359
12	N1 B L100	100	10^{13}	30	100	100.41
13	N4 1	2x40 Dist. 120	$3\ 10^{13}$	20	100	28.686
14	N4 2	2x40 Dist. 125	$3\ 10^{13}$	20	100	28.167
15	N4 3	2x40 Dist. 130	$3\ 10^{13}$	20	100	14.391

Table 1. Run parameters

During the early stage of the pressurization in the nucleated zone (reddish colors), the sill opening results in the decreased fluid pressure around this zone (bluish colors) leading to new nucleation and bubble growth. The location of the narrow yellow ring between these zones corresponds to the radially propagating bubble nucleation front. The front expansion is driven by the "crack waves" resulting from elastic-acoustic coupling on the sill boundaries an propagating along the sill (e.g., B. Chouet, 1986; B. A. Chouet, 1996). The exact cylindrical symmetry is preserved during the sill expansion since the melt and surrounding rocks are homogeneous. The size of the area with the elevated pressure where the bubble are nucleated is about 20 m for the first snapshot and the nucleation front reaches the sill edge (50 meter) during 0.1 s. This means that the nucleation front propagates at the rate of about 0.5 km/s.

Seismic source properties, synthetic seismograms, and their Fourier amplitude spectra for model N1-B are shown in Figure 5. As expected for vertically expanding horizontal sill, the potency tensor is dominated by the ZZ component. Its conversion into seismic moment with equation (17) results in a diagonal tensor with ZZ component approximately three times larger than YY and XX (e.g., pure horizontal tensile crack). All three non-zero moment tensor components are proportional to the ZZ potency function whose time dependence defines the source time function. The body wave displacement and velocity is proportional to its first and second time derivatives, respectively. The latter, shown in Figure 5b is dominated by a low-frequency pulse corresponding to the kinetics of the bubble growth. Much weaker high frequencies correspond to bouncing of the "crack waves" withing the sill (e.g., B. A. Chouet, 1996). Resulting synthetic seismograms (Figure 5c) contain both P and S waves with amplitudes close to the observations. Their frequency content is also close to the observations (Figure 5d). The relatively long coda seen in the observed signal and not reproduced in the synthetic seismograms most likely arises from the scattering of seismic waves within the heterogeneous volcanic media, i.e., from the propagation effect whose explanation would require using a more realistic Green's function.

For other cases with higher N_d values, the nucleation front propagates two (N2 series) and even more than three (N3 series) times faster. The bubble nucleation in the whole sill occurs relatively fast (0.1 s), while the overall duration of the sill expansion

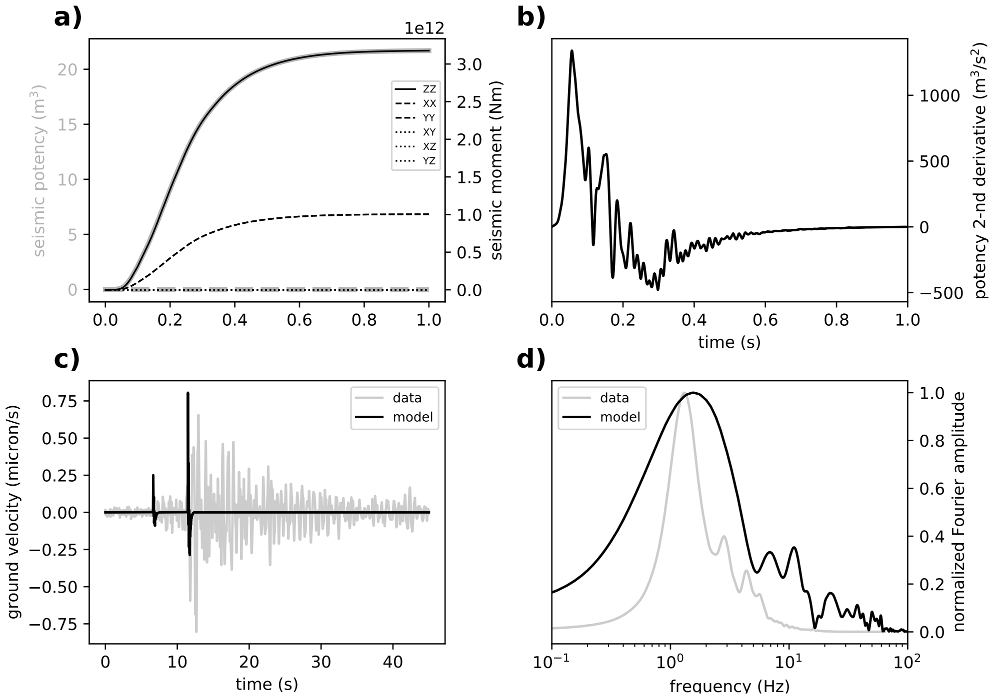

Figure 5. Seismic signature of model N1-B. (a) Components of potency (thick gray lines) and seismic moment (thin black lines) tensors as function of time. (b) Second derivative of the ZZ potency function. (c) Comparison of synthetic and observed seismograms shown with black and gray lines, respectively. East-component seismogram of a DLP earthquake occurred on June 26, 2012 recorded at station LGN located on the slope of the Klyuchevskoy volcano (see supplementary material for details) is shown as “data” (signal was high-passed at 0.5 Hz to remove the microseismic noise. (d) Normalized Fourier amplitudes of signals shown in (c) smoothed in a 1 Hz wide moving window.

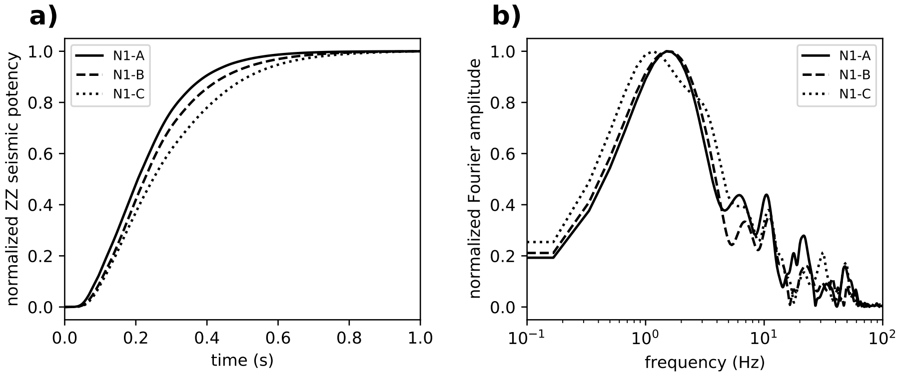

Figure 6. Influence of nucleation threshold ΔP on seismic source time functions. Three considered models differ by the value of this parameter: N1-A 10 kPa, N1-B 30 kPa, N1-C 50 kPa. (a) ZZ components of the seismic potency tensors as function of time. (b) Normalized Fourier amplitude of second derivatives of the ZZ potency function.

vary between 0.2 and 0.8 s for the series of nine model setting (lines 1-9 in Table 1). Therefore, the overall duration is mainly controlled by the kinetics of the bubble growth. The nucleation of new bubbles under appropriate conditions occurs extremely fast and the nucleation time scale is well below the time scale of the front propagation (for the discussed sill size) and future sill pressurization.

The bubbles nucleate when the over-saturation pressure is exceeded (e.g., Hirth et al., 1970). The level of the super-saturation depends on the temperature and a number of melt properties including surface tension, volume, and concentration of water molecules in the melt, as well as distance between them, diffusion coefficient of volatiles at the bubble-melt interface, probability that a nucleus at the top of the barrier will go on to form the new phase, rather than dissolve (Zeldovich factor), and others. With a huge uncertainty of these parameters and difficulties in their experimental constrain, we used three different values of the bubble number density ($N_d = 10^{13}$, 10^{14}, and 10^{15} $1/m^3$) and super-saturation thresholds ($\Delta P = 10$, 30, and 50 kPa), assuming instantaneous nucleation when the target super-saturation is reached. Comparison of time-dependent potency for different simulations demonstrate that the pressurization rate weakly depends on the nucleation threshold, ΔP (Figure 6), and it is strongly affected by the bubble number density,N_d (Figure 7). The general pattern of the evolving pressure is very similar to the one shown in Figure 5, but differs only by the rate of pressurization. The sill expands significantly faster in the case with elevated N_d values.

Two additional simulations (10, 11 in Table 1) were performed to study a possible impact the melt viscosity, which was increased and decreases by an order of magnitude covering the realistic range of the basaltic melt properties. The difference in the pressurization rate (potency increase, not shown here) between these two cases and the model N1-B is negligibly small. The rate of the magma flow becomes important only at high viscosities (above 10^5 Pa s) typical for rhyolitic magmas (Hess & Dingwell, 1996) and controls the rate of sill pressurization.

Similarly to the classical seismological scaling relations we expect stronger event with larger potency (area times opening) proportional to the sill size. For the same pressure inside the sill with radius increased by a factor of two, we expect the sill opening to increase by a factor $\sqrt{2}$, since penny-shaped crack opening is scaled as square root of the disc radius. Together with four times area increase (size in a power two), the potency should increase by a factor $2^{2.5} \approx 5.66$. However, opening of the sill leads to the reduc-

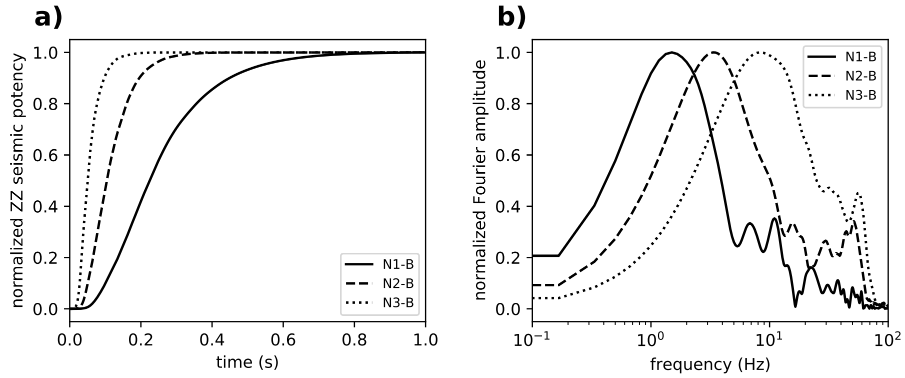

Figure 7. Influence of bubble number density N_d on seismic source time functions. Three considered models differ by the value of this parameter: N1-B 10^{13}, N1-B 10^{14}, N3-B 10^{15}. (a) ZZ components of the seismic potency tensors as function of time. (b) Normalized Fourier amplitude of second derivatives of the ZZ potency function.

tion of the equilibrium pressure of the bubbly magma inside the sill. The results of the model N1-B-L100 show that the potency for the 100 m sill, instead of 50 m, is about 100 m^3 meaning the increase by a factor 5 instead 5.66. The coupling between opening and pressure in the sill leads to a potency-area scaling with slightly deviates from the predictions of the linear elasticity ignoring the pressure-size dependency.

5.2 Configuration with two sills

Expansion of the sill due to the bubble growth and pressurization leads to the deformation of the surrounding elastic media and formation of a relatively wide zone with a reduced pressure clearly seen in the last snapshots of Figure 4. This pressure reduction can initiate bubble nucleation in another sill or magma pocket located at a certain distance within the area of the negative pressure change (blue zone). Three last simulations demonstrate the sensitivity of the secondary nucleation to the distance between two discs (Figure 3b). In order to improve the numerical resolution without significantly increasing the computation time, we slightly decreased the disc radius to 40 m and placed the second disc at three different distances between their centers 130, 120, and 125 m (Table 1) or 50, 40, and 45 m between disc edges. Figure 8 shows the snapshots for the case N4-1. Slightly before 0.3 s the nucleation threshold (20 KPa) is achieved in the disc on the left and the nucleation starts on the right edge of this disc mostly affected by the pressurization of the first disc (snapshot 1 in Figure 8).

Seismic response of a two-sill system is illustrated in Figure 9 for model N4-2 (separation of 125 m). Nucleation of the first sill results in the initial rise of potency/moment values occurring between 0 and 0.3 s. This initial pulse is shorter that for model N1-B (Figure 5) and the dominant frequency higher mainly because of the smaller sill size. The bouncing of “crack waves” expressed in high frequencies seems to be more prominent in such smaller sill. The second sill nucleation starts at 0.6 s. The overall potency increases corresponding to two sills are nearly identical. At the same time, the second derivative of the potency function shows that the second impulse is relatively depleted in high frequencies. The reason for this is that the nucleation of the second sill starts not at the center but at the edge. As a result, the bouncing of “crack waves” is much less efficient.

The time delay for the second sill nucleation strongly depends on the distance between discs as shown in Figure 10. It increases from 0.3 to 0.6 s between separations of 120 ans 125 m. For the 130 m distance between disc centers, the nucleation threshold is never achieved. After the nucleation occurred, the nucleation front propagates toward the opposite edge of the disc with the rate controlled by the bubble growth parameters as discussed above. With pressure growth increase in both discs, the size of zone with a reduced pressure (blue colors) increases and may provoke nucleation in additional magma pockets, not necessarily aligned in the same plane. Vertical cross sections clearly demonstrate significant increase of the negative pressure zone in the Z-direction. Comparison between three cases of the N4 series shows that there exist certain critical distance for the secondary nucleation and the delay time strongly depends on this distance.

6 Discussion and conclusions

We developed an accurate model of generation of seismic waves by the pressure variations caused by bubble growth in the magma. This model is based on a numerical solution of a fluid-elastic coupled equations and includes a bubble nucleation front propagating from initial trigger point in a sill-shaped magma intrusion.

The results of our simulations confirm the hypotheses of O. Melnik et al. (2020) that the rapid growth of gas bubbles within magmatic intrusions can generate seismic waves with amplitudes and spectral content similar to those observed from DLP earthquakes. In particular, we show that with modeling realistic shapes of the intrusions such as sills, a mostly volumetric expansion results in generation of stronger S waves than P waves. Our simulations show that realistic amplitudes can be predicted with modeling sills of ∼50 m of radius and ∼1 m of thickness. The object of such dimensions can correspond either to an individual small sill or to a pocket of oversaturated magma within larger intrusions.

Additionally, our modeling shows that bubble nucleation front propagation is controlled by the coupled elasto-acoustic waves. This propagation is rapid comparing to the kinetics of the bubble growth. The later dominates the source time function and the spectral content of the emitted signals. This kinetics is controlled by the the bubble number density N_d and the gas content in the magma (O. Melnik et al., 2020). The effect of bouncing of "crack waves" eventually leading to resonances of fluid filled cracks (e.g., B. Chouet, 1986; B. A. Chouet, 1996; Maeda & Kumagai, 2017) is rather weak and is not necessary to explain the properties of the observed DLP signals.

The results of our modeling presented in subsection (5.2) highlight a possibility of "interaction" between closely located intrusions when the elastic deformation caused by the degassing/expansion of the first sill can trigger the bubble nucleation in the next closely located magma pocket. We presented simulations for two "interacting" sills. This results can be extrapolated to a case of many closely located magma pockets acting in a cascade. Such behavior can explain the observation of DLP earthquakes often occurring as swarms of many events closely located in time (e.g., White et al., 1996; Shapiro, Droznin, et al., 2017; Song et al., 2023) eventually leading to emergence of deep volcanic tremors (e.g., Aki & Koyanagi, 1981; Soubestre et al., 2019; Journeau et al., 2022).

The emergence of tremors would become favorable in a configuration where many "interacting" pockets of oversaturated magma are closely located. The results shown in Figure 10 demonstrate that with the selected model parameters and in approximation of in-plane circular sills, the interaction becomes possible when inter-sill distance approaches the sill radius. The "interaction" distance would then increase with decreasing the the nucleation threshold. The time delay between two "interacting events" would increase with increasing the inter-sill distance and also with decreasing the bubble number density.

More generally, some scaling relations based on the stress distribution around a pressurized inclusion could be considered. The linear elasticity predicts that the pressure distribution around the inclusion is proportional to the overpressure and decreases as a polynomial function of the ratio $\frac{R}{d}$ (R – disc radius, d – distance from the inclusion center). Near the edge of the inclusion the forth order term, $(\frac{R}{d})^4$, is dominant and defines fast pressure decay away from the inclusion. The width of the zone with the negative pressure is expected to be of the order of the inclusion size. For a given distance, d, from the inclusion, the nucleation occurs when the pressure in the inclusion drops below certain critical value, which linearly increases with the nucleation threshold and decreases as $(\frac{R}{d})^4$, which is the dominant term for the near-field solution.

The presented modeling frameworks can be applied to magma pockets of arbitrary shapes. One possible direction of its application to better understand the origin of deep volcanic tremors would be to investigate the cascading of magma degassing in a system containing many sills and dykes with variable sizes (e.g. O. E. Melnik et al., 2021; Bindeman et al., 2023). A more challenging and important task would be to move from a "static" systems of interacting magma pockets and to model their time evolution and, in particular, their refilling with fresh magma and volatiles which is necessary for functioning of sustained generation of deep volcanic seismicity.

Data availability statement

This study makes no use of input data. The algorithm and its implementation for the 3-D modeling of quasi-static visco-elastic damage rheology are described in Lyakhovsky et al. (2001). The relevant details regarding the execution of model simulations are described in this manuscript. The fortran code used to carry out the calculations as well as the relevant input and output files together with the python scrip used for their visualization are available at the repository:
`https://zenodo.org/records/10409299` (DOI:10.5281/zenodo.10409299).

Acknowledgments
This study was supported by the European Research Council under the European Union Horizon 2020 research and innovation program (Grant Agreement 787399-SEISMAZE).

Appendix A Single bubble growth model

The process of a single bubble growth from a supersaturated magma is described by a set of Raleigh-Lamb equations together with diffusion equations for multiple dissolved volatiles:

$$\frac{\partial}{\partial r}\left(r^2\nu_r\right) = 0;\ \nu_r|_{r=R} = \frac{dR}{dt}; \tag{A1}$$

$$P_g - P_m = \frac{2\sigma}{R} + 4\mu\frac{dR}{dt}\left(\frac{1}{R} - \frac{R^2}{S^3}\right); \tag{A2}$$

$$P_m = P_m^0 + \frac{4}{3}G\left(\frac{S^3 - S_0^3}{S_0^3}\right); \tag{A3}$$

$$\frac{\partial c_s}{\partial t} + \nu_r\frac{\partial c_s}{\partial r} = \frac{1}{r^2}\frac{\partial}{\partial r}\left(D_s r^2\frac{\partial c_s}{\partial r}\right); \tag{A4}$$

$$\frac{4\pi}{3}\frac{d}{dt}\left(R^3\rho_g x_{CO2}^b\right) = 4\pi R^2 J_c; \tag{A5}$$

$$\frac{4\pi}{3}\frac{d}{dt}\left(R^3\rho_g\left(1 - x_{CO2}^b\right)\right) = 4\pi R^2 J_w; \tag{A6}$$

$$J_s = -D_c\rho_m\left(\frac{\partial c_c}{\partial r}\right)_{r=R};\ J_w = -D_w\rho_m\left(\frac{\partial c_w}{\partial r}\right)_{r=R}. \tag{A7}$$

$$\rho_g = \left(\frac{x^b_{CO2}}{\rho_{CO2}\,(P_g,T)} + \frac{1 - x^b_{CO2}}{\rho_{H2O}\,(P_g,T)} \right)^{-1}; \tag{A8}$$

$$\rho_{CO2} = (0.371 + 0.13 \times 10^{-3}T)P_g + 1194.65 - 0.4665T; \tag{A9}$$

$$\rho_{H2O} = (0.22 + 0.13 \times 10^{-3}T)P_g + 892.2 - 0.357T; \tag{A10}$$

$$D_w = c_{H2O} \exp\left(-8.56 - \frac{19110}{T}\right); \tag{A11}$$

$$D_c = \exp\left(-13.99 - \frac{(17367 + 1.945P_g)}{T} + \frac{c_{H2O}(855.2 + 0.271P_g)}{T}\right) \tag{A12}$$

Here t is time, r is the radial coordinate, R is the radius of the bubble, v_r is the radial velocity, index $s = w, c$ corresponds to water and carbon dioxide, respectfully, c_c and c_w are the mass concentrations of CO2 and H2O in the melt, D_c and D_w are the volatile diffusion coefficients, P_g is the pressure of the gas inside the bubble, P_m is the melt pressure, σ is the surface tension, μ is the magma viscosity, S is the radius of the cell, G is the shear modulus of the host rock, ρ_g is the density of the gas in the bubble that depends on the pressure, temperature T and bubble volatile composition x^b_{CO2}.

The densities of pure CO_2 and H_2O are approximated at a limited $P - T$ range using tables produced by NIST Chemistry WebBook (https://webbook.nist.gov/chemistry/).

Diffusion equations (A4) are subjected to two boundary conditions: concentration gradients are equal to zero at the outer surfaces of the cell mimicking symmetry of the system. At $r = R(t)$ volatiles in magma are in chemical equilibrium with the bubble. Thus, $c_s = c_s^{eq}\left(P_g, T, x^b_{CO2}\right)$.

The dynamics of bubble growth under various conditions have been widely discussed in the literature ((Gardner et al., 2023)). Based on the experimental observations we adopt that at the critical supersaturation for the bubble nucleation, the gas pressure, P_0, is several tens of MPa above the pressure of the surrounding melt. This initial pressure difference is compensated by the surface tension term (see equation A2), which decreases as 1/R. This surface tension decrease together with efficient volatile mass flux into the bubbles leads to a steep gas pressure increase. At the later stage the rate of the pressure growth decreases and gas pressure approaches to the equilibrium pressure, P_{eq}.

References

Aki, K., & Koyanagi, R. (1981). Deep volcanic tremor and magma ascent mechanism under kilauea, hawaii. *Journal of Geophysical Research: Solid Earth*, *86*(B8), 7095-7109. Retrieved from `https://agupubs.onlinelibrary.wiley.com/doi/abs/10.1029/JB086iB08p07095` doi: https://doi.org/10.1029/JB086iB08p07095

Aki, K., & Richards, P. G. (2002). *Quantitative seismology* (2nd ed.). University Science Books. Hardcover. Retrieved from `http://www.worldcat.org/isbn/0935702962`

Aso, N., Ohta, K., & Ide, S. (2013). Tectonic, volcanic, and semi-volcanic deep low-frequency earthquakes in western japan. *Tectonophysics*, *600*, 27-40. Retrieved from `https://www.sciencedirect.com/science/article/pii/S0040195112007949` (Great Earthquakes along Subduction Zones) doi: https://doi.org/10.1016/j.tecto.2012.12.015

Aso, N., & Tsai, V. C. (2014). Cooling magma model for deep volcanic long-period earthquakes. *J. Geophys. Res. Solid Earth*, *119*(11), 8442–8456. doi: 10.1002/2014JB011180

Ben-Menahem, A., & Singh, S. J. (2012). *Seismic waves and sources.* Springer Science & Business Media.

Bindeman, I. N., Melnik, O. E., Guillong, M., Utkin, I. S., Wotzlaw, J. F., Schmitt, A. K., & Stern, R. A. (2023). Age of the magma chamber and its physicochemical state under elbrus greater caucasus, russia using zircon petrochronology and modeling insights. *Scientific Reports*, *13*(1), 9733. Retrieved from `https://doi.org/10.1038/s41598-023-36793-y` doi: 10.1038/s41598-023-36793-y

Burgisser, A., Alletti, M., & Scaillet, B. (2015, Apr). *D-compress.* Retrieved from `https://theghub.org/resources/3791`

Cassidy, M., Manga, M., Cashman, K., & Bachmann, O. (2018). Controls on explosive-effusive volcanic eruption styles. *Nature Communications*, *9*(1), 2839. Retrieved from `https://doi.org/10.1038/s41467-018-05293-3` doi: 10.1038/s41467-018-05293-3

Chouet, B. (1986). Dynamics of a fluid-driven crack in three dimensions by the finite difference method. *Journal of Geophysical Research: Solid Earth*, *91*(B14), 13967-13992. Retrieved from `https://agupubs.onlinelibrary.wiley.com/doi/abs/10.1029/JB091iB14p13967` doi: https://doi.org/10.1029/JB091iB14p13967

Chouet, B., Dawson, P., & Arciniega-Ceballos, A. (2005). Source mechanism of vulcanian degassing at popocatépetl volcano, mexico, determined from waveform inversions of very long period signals. *Journal of Geophysical Research: Solid Earth*, *110*(B7). Retrieved from `https://agupubs.onlinelibrary.wiley.com/doi/abs/10.1029/2004JB003524` doi: https://doi.org/10.1029/2004JB003524

Chouet, B., Dawson, P., & Nakano, M. (2006). Dynamics of diffusive bubble growth and pressure recovery in a bubbly rhyolitic melt embedded in an elastic solid. *Journal of Geophysical Research: Solid Earth*, *111*(B7). Retrieved from `https://agupubs.onlinelibrary.wiley.com/doi/abs/10.1029/2005JB004174` doi: https://doi.org/10.1029/2005JB004174

Chouet, B. A. (1996). Long-period volcano seismicity: its source and use in eruption forecasting. *Nature*, *380*, 309-316. doi: 10.1038/380309a0

Cundall, P. A. (1988). Numerical experiments on localization in frictional materials. In *Proc. of the workshop on limit analysis and bifurcation theory.*

Fedotov, S. A., Zharinov, N. A., & Gontovaya, L. I. (2010). The magmatic system of the klyuchevskaya group of volcanoes inferred from data on its eruptions, earthquakes, deformation, and deep structure. *J. Volcanol. Geotherm. Res.*, *4*(1), 1–33. doi: 10.1134/S074204631001001X

Galina, N. A., Shapiro, N. M., Droznin, D. V., Droznina, S. Y., Senyukov, S. L., & Chebrov, D. V. (2020). Recurrence of deep long-period earthquakes beneath the Klyuchevskoi volcano group, Kamchatka. *Izvestiya, Physics of the Solid Earth*, *56*(6), 749–761. doi: 10.1134/S1069351320060026

Gardner, J. E., Wadsworth, F. B., Carley, T. L., Llewellin, E. W., Kusumaatmaja, H., & Sahagian, D. (2023). Bubble formation in magma. *Annual Review of Earth and Planetary Sciences*, *51*, 131–154. doi: https://doi.org/10.1146/annurev-earth-031621-080308

Greenfield, T., Winder, T., Rawlinson, N., Maclennan, J., White, R. S., Ágústsdóttir, T., … Horálek, J. (2022). Deep long period seismicity preceding and during the 2021 fagradalsfjall eruption, iceland. *Bulletin of Volcanology*, *84*(12), 101. Retrieved from `https://doi.org/10.1007/s00445-022-01603-2` doi: 10.1007/s00445-022-01603-2

Hensch, M., Dahm, T., Ritter, J., Heimann, S., Schmidt, B., Stange, S., & Lehmann, K. (2019, 01). Deep low-frequency earthquakes reveal ongoing magmatic recharge beneath Laacher See Volcano (Eifel, Germany). *Geophysical Journal International*, *216*(3), 2025-2036. doi: 10.1093/gji/ggy532

Hess, K., & Dingwell, D. B. (1996). Viscosities of hydrous leucogranitic melts: A non-arrhenian model. *American Mineralogist: Journal of Earth and Planetary Materials*, *81*(9-10), 1297–1300.

Hirth, J., Pound, G., & St. Pierre, G. (1970). Bubble nucleation. *Metallurgical Transactions*, *1*, 939–945. doi: https://doi.org/10.1007/BF02811776

Ikegaya, T., & Yamamoto, M. (2021). Spatio-temporal characteristics and focal mechanisms of deep low-frequency earthquakes beneath the zao volcano, northeastern japan. *Journal of Volcanology and Geothermal Research*, *417*, 107321. Retrieved from https://www.sciencedirect.com/science/article/pii/S0377027321001505 doi: https://doi.org/10.1016/j.jvolgeores.2021.107321

Jaupart, C., & Vergniolle, S. (1988). Laboratory models of hawaiian and strombolian eruptions. *Nature*, *331*(6151), 58–60. Retrieved from https://doi.org/10.1038/331058a0 doi: 10.1038/331058a0

Journeau, C., Shapiro, L., N. M.and Seydoux, Soubestre, J., Koulakov, I. Y., Jakovlev, A. V., Abkadyrov, I., … Jaupart, C. (2022). Seismic tremor reveals active trans-crustal magmatic system beneath Kamchatka volcanoes. *Sci. Adv.*, *8*(5), eabj1571. doi: 10.1126/sciadv.abj1571

Koulakov, I., Shapiro, N. M., Sens-Schönfelder, C., Luehr, B. G., Gordeev, E. I., Jakovlev, A., … Stupina, T. (2020). Mantle and crustal sources of magmatic activity of Klyuchevskoy and surrounding volcanoes in Kamchatka inferred from earthquake tomography. *Journal of Geophysical Research: Solid Earth*, *125*(10), e2020JB020097. doi: 10.1029/2020JB020097

Kurihara, R., & Obara, K. (2021). Spatiotemporal characteristics of relocated deep low-frequency earthquakes beneath 52 volcanic regions in japan over an analysis period of 14 years and 9 months. *J. Geophys. Res. Solid Earth*, *126*(10), e2021JB022173. doi: 10.1029/2021JB022173

Kurihara, R., Obara, K., Takeo, A., & Tanaka, Y. (2019). Deep low-frequency earthquakes associated with the eruptions of shinmoe-dake in kirishimavolcanoes. *J. Geophys. Res. Solid Earth*, *124*(12), 13079-13095. doi: 10.1029/2019JB018032

Lensky, N. G., Niebo, R. W., Holloway, J. R., Lyakhovsky, V., & Navon, O. (2006). Bubble nucleation as a trigger for xenolith entrapment in mantle melts. *Earth and Planetary Science Letters*, *245*(1), 278-288. Retrieved from https://www.sciencedirect.com/science/article/pii/S0012821X06002135 doi: https://doi.org/10.1016/j.epsl.2005.11.064

Levin, V., Droznina, S. Y., Gavrilenko, M., Carr, M. J., & Senyukov, S. L. (2014). Seismically active subcrustal magma source of the klyuchevskoy volcano in kamchatka, russia. *Geol.*, *42*(11), 983-986. doi: 10.1130/G35972.1

Lu, L., & Bostock, M. G. (2022). Deep long-period earthquakes near mount meager, british columbia. *Canadian Journal of Earth Sciences*, *59*(7), 407-417. Retrieved from https://doi.org/10.1139/cjes-2021-0103 doi: 10.1139/cjes-2021-0103

Lyakhovsky, V., Ben-Zion, Y., Ilchev, A., & Mendecki, A. (2016). Dynamic rupture in a damage-breakage rheology model. *Geophysical Journal International*, *206*(2), 1126-1143. Retrieved from https://doi.org/10.1093/gji/ggw183 doi: 10.1093/gji/ggw183

Lyakhovsky, V., Hurwitz, S., & Navon, O. (1996). Bubble growth in rhyolitic melts: experimental and numerical investigation. *Bulletin of Volcanology*, *58*(1), 19–32. Retrieved from https://doi.org/10.1007/s004450050122 doi: 10.1007/s004450050122

Lyakhovsky, V., Ilchev, A., & Agnon. (2001). Modeling of damage and instabilities of rock mass by means of a non-linear rheological model. In G. Van Aswegen, R. J. Durrheim, & W. D. Ortlepp (Eds.), *Dynamic rock mass response to mining* (pp. 413–420). South African Institute of Mining and Metallurgy.

Maeda, Y., & Kumagai, H. (2017). A generalized equation for the resonance frequencies of a fluid-filled crack. *Geophysical Journal International*, *209*(1), 192–201. doi: 10.1093/gji/ggx019

Melnik, O., Lyakhovsky, V., Shapiro, N., Galina, N., & Bergal-Kuvikas, O. (2020). Deep long period volcanic earthquakes generated by degassing of volatile-rich basaltic magmas. *Nature Communications*, *11*(1), 3918. Retrieved from `https://doi.org/10.1038/s41467-020-17759-4` doi: 10.1038/s41467-020-17759-4

Melnik, O. E., Utkin, I. S., & Bindeman, I. N. (2021). Magma chamber formation by dike accretion and crustal melting: 2d thermo-compositional model with emphasis on eruptions and implication for zircon records. *Journal of Geophysical Research: Solid Earth*, *126*(12), e2021JB023008. Retrieved from `https://agupubs.onlinelibrary.wiley.com/doi/abs/10.1029/2021JB023008` (e2021JB023008 2021JB023008) doi: https://doi.org/10.1029/2021JB023008

Mironov, N., & Portnyagin, M. (2011). H2o and co2 in parental magmas of kliuchevskoi volcano inferred from study of melt and fluid inclusions in olivine. *Russian Geology and Geophysics*, *52*(11), 1353-1367. Retrieved from `https://www.sciencedirect.com/science/article/pii/S1068797111002161` (Melts and Fluids in Natural Mineral and Ore Formation Processes: Modern Studies of Fluid and Melt Inclusions in Minerals) doi: https://doi.org/10.1016/j.rgg.2011.10.007

Nichols, M., Malone, S., Moran, S., Thelen, W., & Vidale, J. (2011). Deep long-period earthquakes beneath washington and oregon volcanoes. *J. Volcanol. Geotherm. Res.*, *200*(3), 116-128. doi: 10.1016/j.jvolgeores.2010.12.005

Nishimura, T. (2004). Pressure recovery in magma due to bubble growth. *Geophysical Research Letters*, *31*(12). Retrieved from `https://agupubs.onlinelibrary.wiley.com/doi/abs/10.1029/2004GL019810` doi: https://doi.org/10.1029/2004GL019810

Papale, P. (1999). Modeling of the solubility of a two-component h2o+ co2 fluid in silicate liquids. *American Mineralogist*, *84*(4), 477–492. doi: https://doi.org/10.2138/am-1999-0402

Pitt, A. M., & Hill, D. P. (1994). Long-period earthquakes in the long valley caldera region, eastern california. *Geophysical Research Letters*, *21*(16), 1679-1682. Retrieved from `https://agupubs.onlinelibrary.wiley.com/doi/abs/10.1029/94GL01371` doi: https://doi.org/10.1029/94GL01371

Poliakov, A. N. B., Cundall, P. A., Podladchikov, Y. Y., & Lyakhovsky, V. A. (1993). An explicit inertial method for the simulation of viscoelastic flow: an evaluation of elastic effects on diapiric flow in two-and three-layers models. In *Flow and creep in the solar system: observations, modeling and theory* (pp. 175–195). Springer.

Portnyagin, M., Hoernle, K., Plechov, P., Mironov, N., & Khubunaya, S. (2007). Constraints on mantle melting and composition and nature of slab components in volcanic arcs from volatiles (h2o, s, cl, f) and trace elements in melt inclusions from the kamchatka arc. *Earth and Planetary Science Letters*, *255*(1), 53-69. Retrieved from `https://www.sciencedirect.com/science/article/pii/S0012821X06008727` doi: https://doi.org/10.1016/j.epsl.2006.12.005

Portnyagin, M., Mironov, N., Botcharnikov, R., Gurenko, A., Almeev, R. R., Luft, C., & Holtz, F. (2019). Dehydration of melt inclusions in olivine and implications for the origin of silica-undersaturated island-arc melts. *Earth and Planetary Science Letters*, *517*, 95-105. Retrieved from `https://www.sciencedirect.com/science/article/pii/S0012821X19302250` doi: https://doi.org/10.1016/j.epsl.2019.04.021

Power, J., Stihler, S., White, R., & Moran, S. (2004). Observations of deep long-period (dlp) seismic events beneath aleutian arc volcanoes; 1989–2002. *J. Volcanol. Geotherm. Res*, *138*(3), 243–266. doi: 10.1016/j.jvolgeores.2004.07.005

Shapiro, N. M., Droznin, D. V., Droznina, S. Y., Senyukov, S. L., Gusev, A. A.,

& Gordeev, E. I. (2017). Deep and shallow long-period volcanic seismicity linked by fluid-pressure transfer. *Nat. Geosci.*, *10*(6), 442–445. doi: 10.1038/ngeo2952

Shapiro, N. M., Sens-Schönfelder, C., Lühr, B. G., Weber, M., Abkadyrov, I., Gordeev, E. I., … Saltykov, V. A. (2017). Understanding kamchatka's extraordinary volcano cluster. *Eos*, *98*. doi: 10.1029/2017EO071351

Shea, T. (2017). Bubble nucleation in magmas: a dominantly heterogeneous process? *Journal of Volcanology and Geothermal Research*, *343*, 155–170. doi: https://doi.org/10.1016/j.jvolgeores.2017.06.025

Song, Z., Tan, Y. J., & Roman, D. C. (2023). Deep long-period earthquakes at akutan volcano from 2005 to 2017 better track magma influxes compared to volcano-tectonic earthquakes. *Geophysical Research Letters*, *50*(10), e2022GL101987. Retrieved from `https://agupubs.onlinelibrary.wiley.com/doi/abs/10.1029/2022GL101987` (e2022GL101987 2022GL101987) doi: https://doi.org/10.1029/2022GL101987

Soubestre, J., Seydoux, L., Shapiro, N. M., de Rosny, J., Droznin, D. V., Droznina, S. Y., … Gordeev, E. I. (2019). Depth migration of seismovolcanic tremor sources below the klyuchevskoy volcanic group (kamchatka) determined from a network-based analysis. *Geophysical Research Letters*, *46*(14), 8018-8030. Retrieved from `https://agupubs.onlinelibrary.wiley.com/doi/abs/10.1029/2019GL083465` doi: https://doi.org/10.1029/2019GL083465

Sparks, R. S. J. (1978). The dynamics of bubble formation and growth in magmas: a review and analysis. *Journal of Volcanology and Geothermal Research*, *3*(1-2), 1–37. doi: https://doi.org/10.1016/0377-0273(78)90002-1

Ukawa, M., & Ohtake, M. (1987). A monochromatic earthquake suggesting deep-seated magmatic activity beneath the izu-ooshima volcano, japan. *J. Geophys. Res. Solid Earth*, *92*(B12), 12649-12663. doi: 10.1029/JB092iB12p12649

Wallace, P. J., Plank, T., Edmonds, M., & Hauri, E. H. (2015). Chapter 7 - volatiles in magmas. In H. Sigurdsson (Ed.), *The encyclopedia of volcanoes (second edition)* (Second Edition ed., p. 163-183). Amsterdam: Academic Press. Retrieved from `https://www.sciencedirect.com/science/article/pii/B9780123859389000079` doi: https://doi.org/10.1016/B978-0-12-385938-9.00007-9

Wech, A. G., Thelen, W. A., & Thomas, A. M. (2020). Deep long-period earthquakes generated by second boiling beneath mauna kea volcano. *Science*, *368*(6492), 775-779. doi: 10.1126/science.aba4798

White, R. A., Newhall, C. G., & Punongbayan, R. S. (1996). Precursory deep long-period earthquakes at mount pinatubo: Spatio-temporal link to a basalt trigger. *Fire and mud: Eruptions and lahars of Mount Pinatubo, Philippines*, 307–328.

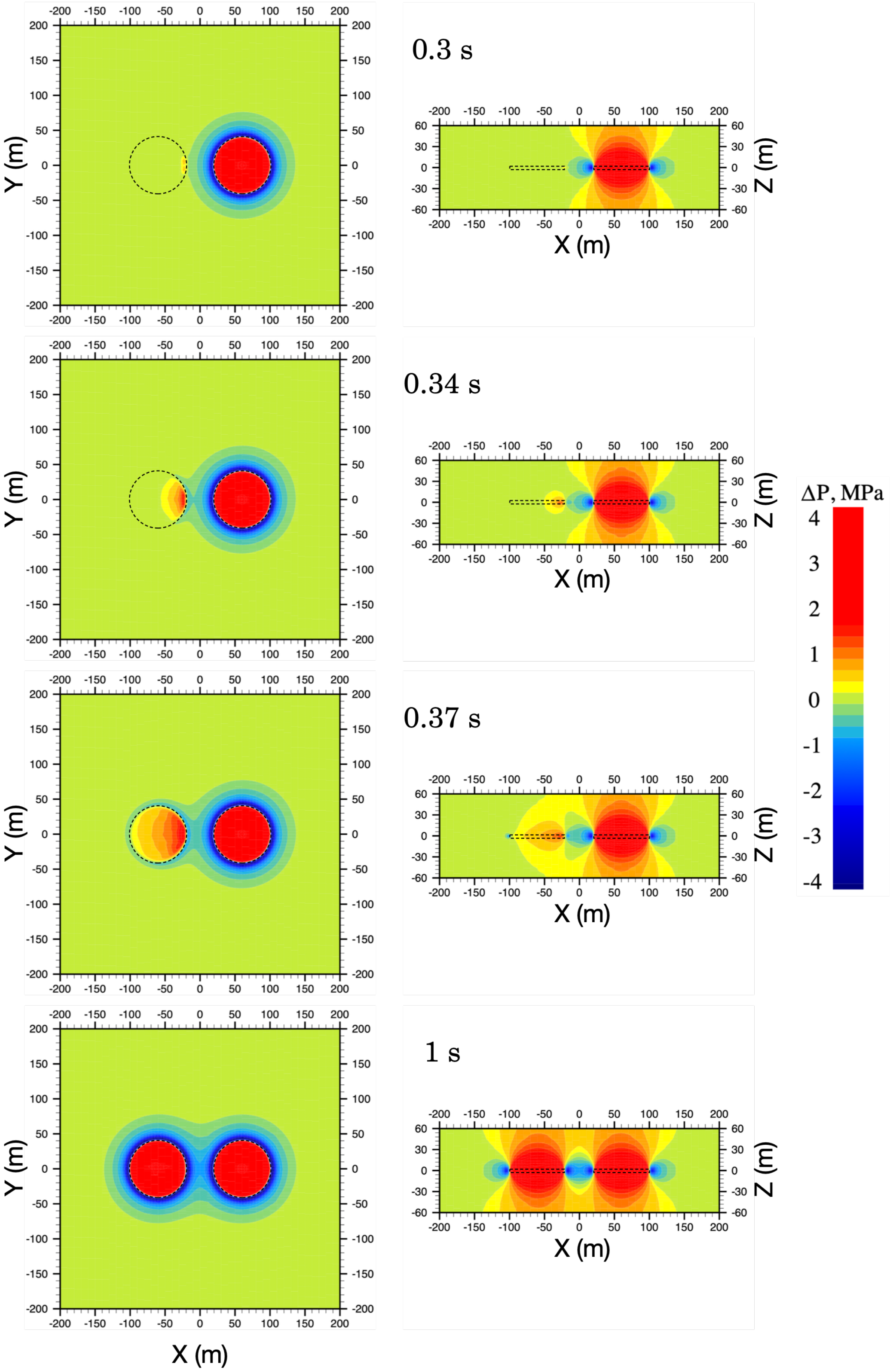

Figure 8. Snapshots of pressure evolution in time in a model with two interacting sills (distance 120 m, model N4-1). Left and right frames show horizontal and vertical cross-sections at Z=0 and Y=0, respectively. Times are indicated above the frames. Dashed lines indicate the boundaries of the magmatic sill.

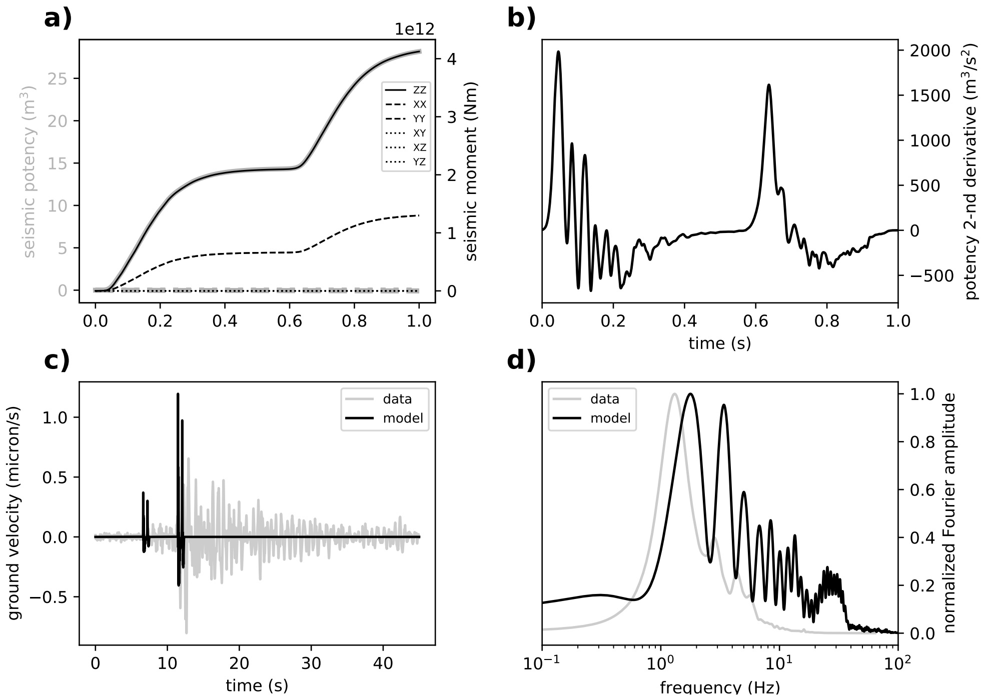

Figure 9. Similar to Figure 5 but model N4-2.

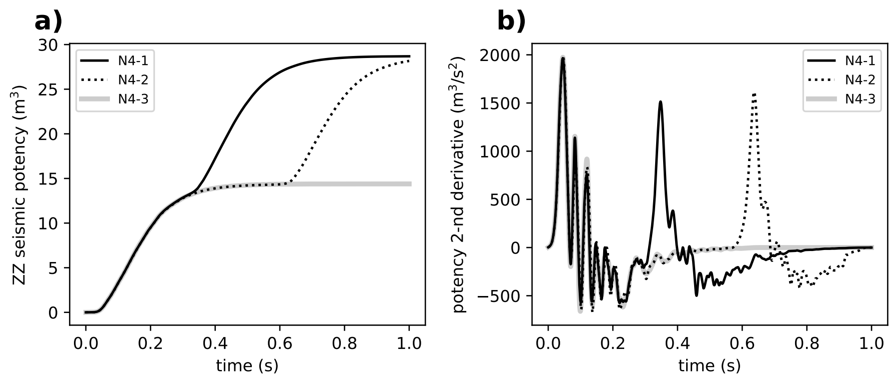

Figure 10. Comparison of seismic source time functions for models with two sills. (a) ZZ components of the seismic potency tensors as function of time. (b) Second derivatives of the ZZ potency function.